Messier 87: A Laboratory for Exploring AGN Variability using the Event Horizon Telescope

by

Britton Jeter

A thesis
presented to the University of Waterloo
in fulfillment of the
thesis requirement for the degree of
Doctor of Philosophy
in
Physics

Waterloo, Ontario, Canada, 2020

Examining Committee Membership

The following served on the Examining Committee for this thesis. The decision of the Examining Committee is by majority vote.

External Examiner:	Christopher Reynolds Professor, Institute of Astronomy Cambridge University
Supervisor(s):	Avery E. Broderick Associate Professor, Dept. of Physics and Astronomy University of Waterloo Brian McNamara Professor, Dept. of Physics and Astronomy University of Waterloo
Internal Member(s):	Niayesh Afshordi Associate Professor, Dept. of Physics and Astronomy University of Waterloo Luis Lehner Professor, Perimeter Institute
Internal-External Member:	Francis Poulin Professor, Dept. of Applied Mathematics University of Waterloo

Author's Declaration

This thesis consists of material all of which I authored or co-authored: see Statement of Contributions included in the thesis. This is a true copy of the thesis, including any required final revisions, as accepted by my examiners.

I understand that my thesis may be made electronically available to the public.

Statement of Contributions

Chapters 2 and 3 contain original research written by myself, Britton Jeter. Chapter 2 and sections of Chapter 3 have been published in the peer-reviewed journals Monthly Notices of the Royal Astronomical Society (MNRAS) and the Astrophysical Journal (ApJ) respectively. The paper references are:

Jeter, Britton; Broderick, Avery E.; Gold, Roman, 2020, Monthly Notices of the Royal Astronomical Society, Volume 493, Issue 4, p.5606-5616, doi: 10.1093/mnras/staa679

Jeter, Britton; Broderick, Avery E.; McNamara, B. R, 2019, The Astrophysical Journal, Volume 882, Issue 2, article id. 82, 11 pp. doi: 10.3847/1538-4357/ab3221

In each of these publications, I, Britton Jeter, am the first author, having analyzed the data and written the manuscript. The second author, Dr. Avery E. Broderick, is my supervisor. The other co-authors are collaborators who provided useful discussion and provided comments on how to improve the manuscripts before publication.

Abstract

At a distance of 50 million light years at the heart of the Virgo cluster, lies the giant elliptical galaxy Messier 87. This galaxy has at its center a brilliant relativistic jet, observable at all wavelengths, and at the jet's base, the black hole M87*. As of April 2017, this black hole was directly imaged by the Event Horizon Telescope (EHT), a network of eight radio telescopes scattered across the globe. These first images of a black hole will let us investigate not only the physics of black holes, but also the formation and launching mechanism of relativistic jets. The jet in M87 is known to exhibit variability on many different time-scales, from weeks to decades, and comparing the images produced by the EHT to models for jet variability will let us learn how relativistic jets are born.

Synchrotron spot models have been used to model variability near black holes; the first part of this thesis extends these models by allowing spots to shear and deform in the jet velocity field. Depending on the position of the spot, shearing forces can significantly alter the structure of the spot, producing distinct signals in reconstructed images and light curves. The maximum intensity of the shearing spot can vary by as much as a factor of five depending on the spot azimuthal launch position, but the intensity decay time depends most significantly on the spot radial launch position. Spots launched by a black hole driven jet exhibit distinct arc structures in reconstructed images, and exhibit brighter and shorter-lived enhancements of the light curve. Spots launched by a wind-driven jet have exhibit much simpler structures in the image, and longer-lived light curve enhancements than spots launched by a black hole driven jet.

The EHT measured the mass of M87* to be $6.5 \times 10^9\ M_\odot$, consistent with previous mass estimates from stellar kinematics, but inconsistent by up to 2σ with mass estimates made using gas dynamics models of the gas disk at parsec scales. Critical to gas-dynamical modeling is the assumed underlying dynamical state of the gas: that it lies on circular Keplerian orbits, potentially with some additional turbulent pressure support. This is inconsistent with models of the gas flow about low-accretion-rate SMBHs and at odds with observations of the Galactic Center.

In the second part of this thesis, I present an extended model for non-Keplerian gas disks and explore their implications for SMBH mass measurements. I show that a larger central black hole with gas experiencing small amounts of sub-Keplerian motion and/or non-trivial disk thicknesses can produce velocity curves similar to models that just contain circular Keplerian motions and a lower black hole mass. These non-Keplerian models are distinguishable from low-mass Keplerian models primarily through measuremnets of the velocity dispersion, wherein non-Keplerian models produce higher and narrower peak dispersions. By combining the existing velocity measurements from Walsh et al. (2013) and

the EHT mass estimate, we place constraints on the gas disk inclination and sub-Keplerian fraction. These constraints require the parsec-scale ionized gas disk be misaligned with the masradio jet by at least 2°, and more typically 15°. Modifications to the gas dynamics model either by introducing sub-Keplerian velocities or thick disks produces further misalignment with the radio jet. If the jet is driven by the black hole spin, this implies that the angular momentum of the black hole is decoupled with the angular momentum of the large scale gas feeding M87*. The velocity model presented in this thesis is capable of resolving the discrepancy between the ionized gas dynamics and stellar kinematics mass estimates, and is applicable to gas-dynamical mass estimates of SMBHs in general.

Acknowledgements

I would like to thank my supervisor Avery Broderick for providing his support, patience, and guidance for my lengthy time as a graduate student. I also want to thank the other graduate students at Perimeter and Waterloo for helpful discussion and priceless camaraderie, who helped me feel part of a wonderful community. I also have to thank my Mom, Dad, and my sister Claire, for always letting me choose my own path, and for always giving me love and encouragement.

Table of Contents

List of Figures

Chapter 1

Introduction to Active Galactic Nuclei

The center of every galaxy houses a supermassive black hole, an object so massive and compact that even light must succumb to its pull. These objects used to live only in chalkboards and notebooks for decades after the first solutions to Einstein's field equations emerged (Schwarzschild, 1916), but the study of extragalactic astronomy suggested they might exist off the page as well.

Seyfert galaxies and Quasars are two large subclasses of galaxies which exhibit tremendous luminosities and energetic phenomena from their galaxy centers. The centers of these galaxies produces as much light as the host galaxy itself, and in the case of quasars, can be orders of magnitude brighter than the host galaxy. The extreme energetics of these active galactic nuclei (AGN) cannot easily be attributed to starlight, and early studies of Seyferts showed that all this emission must come from a region within 100 parsecs of their galactic centers. The dispersion of the emission lines from Seyfert spectra suggest the gas is gravitationally bound to objects that are at least a million times the mass of our Sun (Seyfert, 1943).

Quasars, or quasi-stellar objects, are bright, extragalactic point sources on the sky. They are known to be very distant objects, with most active at a cosmological redshift near 2. All AGN are variable to some degree, especially quasars, meaning their luminosity changes over time. The variability timescale for quasars ranges from a few months to a few days, meaning that in the later case much of their energy must come from a region spanning only a few light-days. As mentioned above, Quasars regularly exceed the apparent magnitude of their host galaxies, for example, the quasar 3C 279 has an estimated

bolometric luminosity of at least 10^{12} $L_{\odot}$, or 10^{45} erg/s (Beckmann et al., 2006), 100 times brighter than the Milky Way.

Seyferts and Quasars are catalogued and studied primarily at optical wavelengths, but these AGN also emit at all other frequencies. AGN with large radio components are of particular interest, since the brightest of these radio-loud AGN also produce vast astrophysical jets, sometimes extending out to Mpc distances. Assuming these large-scale radio features are powered by the terminations shocks of these jets against the intergalactic medium, their energy content lies anywhere from 10^{41} to 10^{48} ergs^{-1}, rivaling their electromagnetic luminosities.

In order to explain the extreme luminosities of AGN, and resolve the paradox of such small emitting regions, supermassive black holes (SMBH) have become the favored theoretical engine (Lynden-Bell, 1969). By winding up magnetic fields coupled to the black hole spin, or by producing an intensely hot accretion disk with strong winds, these black holes can produce the required kinetic and electromagnetic energies needed to power AGN in Quasars and Seyfert galaxies, and propel galactic jets.

SMBH masses are strongly correlated with their host galaxy properties, including the velocity dispersion of bulge stars σ (Ferrarese & Merritt, 2000; Gebhardt et al., 2000), and total luminosity of the bulge (Kormendy & Richstone, 1995; Marconi & Hunt, 2003), and subsequent correlations with halo mass (Kormendy & Bender, 2011), and even the total number of globular clusters (Burkert & Tremaine, 2010; Harris & Harris, 2011). These correlations are believed to arise due to feedback mechanisms associated with the AGN phase, through which SMBHs play a critical role in regulating the growth and evolution of their hosts (see, e.g., McNamara & Nulsen, 2012; Fabian, 2012). AGN feedback on galaxy evolution is a critical component that helps regulate star formation, where the large scale jet helps heat intergalactic gas to prevent runaway cooling and move gas inside the galaxy outwards.

It is still not clear how exactly these supermassive black holes feed, and how exactly they form and accelerate their tremendous jets. Until 2017, no telescope was able to see into the immediate surroundings of a black hole, where the in-falling gas interacts with the black hole to produce a jet. By using 8 stations stations at 6 sites, radio dishes scattered all over the globe to produce a virtual telescope the size of the Earth, the first resolved images of the black hole at the center of the giant elliptical galaxy M87 were produced. The Event Horizon Telescope (EHT) Collaboration hopes to continue taking images of M87's black hole, M87*, as well as the black hole at the center of our own galaxy, Sagittarius A* (Sgr A*). By utilizing repeated observations, it should be possible to determine the precise jet launching mechanism in M87*, especially if the EHT captures one of M87*'s

more energetic outbursts.

1.1 M87 as AGN Laboratory

This jet is the most prominent feature of M87 beyond the horizon, extending to scales of 40 kpc (Junor et al., 1999; Ly et al., 2007; Sparks et al., 1996). The luminosity of M87's jet roughly 10^{44} erg s^{-1} as measured at a few different locations. On kiloparsec scales observations of X-ray cavities inflated by the jet can be used to estimate jet power to about 10^{43} erg s^{-1} to 10^{44} erg s^{-1} with timescales of approximately 1 Myr (Young et al., 2002). Below kiloparsec scales, superluminal optical features in the jet can be used to estimate the jet power, assuming they are the products of shocks. The bright feature Knot A sits 0.9 kpc from the jet base and exhibits superluminal velocities up to 1.6c (Meyer et al., 2013) and yields and estimated jet power of a few$\times 10^{44}$ erg s^{-1} (Bicknell & Begelman, 1996) on a timescale of 10^3 years. The bright optical feature HST 1 sits 60 pc from the jet base, and contains superluminal features with velocities up to 6c (Giroletti et al., 2012). On timescales of 30 years, this feature yet again yields and estimated jet power of 10^{44} erg s^{-1} (Stawarz et al., 2006; Bromberg & Levinson, 2009).

Prior VLBI observations have localized the jet to the near-horizon region (Junor et al., 1999; Ly et al., 2007; Sparks et al., 1996). Phased-reference observations, which permit VLBI-resolution astrometric observations, have verified that the relativistic jet photosphere converges on a single point at high frequencies (Hada et al., 2011), with a jet width that decreases as a power-law with height, consistent with analytical expectations (Blandford & Königl, 1979). Previous EHT measurements of the size of the launching region have subsequently identified the emission region as the launch site for the jet, favoring a black hole as a source (Doeleman et al., 2008, 2012).

VLBI movies of M87 show clear evidence of time-dependent structure in the jet near the black hole (Ly et al., 2007; Walker et al., 2016; Hada et al., 2016). Multi-epoch imaging at 43 GHz over five years shows clear evidence of jet features with substantial proper motions. A faint but visible counter-jet exists within 0.5 mas of the jet core on the eastern side, with variable components moving away from the core at approximately 0.17c. The western side of the jet is much brighter, with two clear limb-brightened arms on the north and south. These arms contain smaller jet components with apparent velocities between 0.25c and 0.4c, but are most likely completely different components between observing epochs (Ly et al., 2007). Similar observations at 86 GHz also exhibit similar jet components, and with definite variability over 4 months of observations. These higher frequency observations also see a weak, highly variable counter-jet within 0.25 mas of the jet core, also with proper motions of

approximately 0.17c. A pair of limb-brightened arms extend westward of the jet core, with multiple jet components in both the north and south arm. These components have apparent velocities between 0.1c and 0.48c, with proper motions approximately 1.0 mas yr^{-1} to 1.81 mas yr^{-1}, with new components appearing on a timescale of a few months (Hada et al., 2016).

While these low-frequency observations have been very successful at characterizing the motion of these components at the mas scale, it is not clear how these components are formed and launched. By finally resolving the horizon-scale structure of the M87 nucleus, it should be possible to determine the jet-launching structure. It should then be possible to determine whether M87's jet is powered by the black hole itself, or from relativistic winds driven off the accretion disk.

1.2 Jet Launching Mechanisms

The extreme luminosity of AGN jets are thought to originate from the conversion of gravitational potential energy to radiation from deep inside the the potential well of supermassive black holes. The mechanism of this conversion is unconfirmed, though at present is believed to be facilitated by the extraction of rotational energy via magnetic torques, the chief distinguishing factor being the energy reservoir and topology of the magnetic fields. These may be organized into two primary classes: jets driven by black holes (Blandford & Znajek, 1977) and jets driven by accretion flows (Blandford & Payne, 1982). In the former, the jet is powered by the extraction of rotational energy via large-scale electromagnetic fields near the horizon of the supermassive black hole, which become highly collimated far from the black hole. In the latter, the outflows are associated with a massive disk wind emanating from a hot accretion disk around the black hole, where the disk electromagnetic fields provide the motive force and the disk particles provides the luminous material.

More concretely, when a spinning black hole is threaded by magnetic field lines from an external accretion disk, and the fields are strong enough, the potential difference becomes substantial enough to break-down the vacuum and generate a pair-production cascade. This will result in the formation of a force-free magnetosphere around the black hole, which will extract rotational energy from the black hole and convert it to an electro-magnetic flux. For parabolic magnetic fields roughly parallel to the black hole rotation axis at infinity, the black hole luminosity L_{BH} will be approximately

$$L_{BH} = 10^{45}\ a^2 \dot{M}\ \mathrm{erg/s}, \tag{1.1}$$

where a is the spin of the black hole, and $\dot{M}$ is the accretion rate in $M_\odot/yr$. This requires a magnetic field strength of

$$B \approx 0.2 \left(\frac{L_{BH}}{10^{45} \text{ erg/s}} \right)^{-1/2} a^{-1} \left(\frac{M}{10^9 \ M_\odot} \right)^{-1} \text{ T.} \tag{1.2}$$

In order to satisfy the condition for pair production, the magnetic field strength must be larger than

$$B_{pp} > 20 \ a^{-3/4} \left(\frac{M}{M_\odot} \right)^{-1/2} \text{ T.} \tag{1.3}$$

For M87, with a jet luminosity of 10^{44} erg/s and a mass of $6.5 \times 10^9 \ M_\odot$, this corresponds to a magnetic field strength of $B \approx 0.097 \ a^{-1}$ T, which satisfies the pair production requirement of $B_{pp} = 2.5 \times 10^{-4} a^{-3/4}$ T. Assuming the magnetic field structure around M87 follows the same parabolic shape as the millimeter-wavelength radio jet, a black-hole driven jet for M87 is not unphysical.

Instead of extracting energy from the black hole, magnetic fields threading the accretion can also extract energy from the accretion disk itself. Supported by centrifugal torques, and launched by a hot, magnetically dominated corona, large matter, energy, and angular momentum fluxes can be generated by the accretion disk in the form of jets collimated by the toroidal magnetic fields in the outer disk. For magnetic field strengths in the disk between 0.01 and 1 T, typical MHD solutions yield luminosities between 10^{41} and 10^{46} erg/s^{-1}, as well as relativistic velocities in the jet at large distances from the accretion disk. Due to the high jet velocities and appropriate luminosity, it is also possible that M87's jet could be driven by the accretion disk alone, but magnetic turbulence and thermal instabilities may be enough to prevent a significant disk-driven jet.

In either case, the structure of the resulting jet is very similar. The canonical jet model extracted from simulations features a force-free interior where the majority of the electromagnetic energy density is uncoupled from any particles in the jet (McKinney, 2006; Hawley & Krolik, 2006; Tchekhovskoy et al., 2008). The exterior of the jet is composed of a magnetically dominated wind where the magnetic pressure is much larger than the gas pressure. Both of these regions are, in turn, supported by a hot, thick accretion flow which provides the currents for the magnetic fields.

1.3 Force-Free Jet

Simulated EHT images, which show sub-horizon scale emission structure, have been produced using a simplified, stationary, force-free model of the jet-interior (Broderick & Loeb,

2009). This jet model qualitatively reproduces most of the field and velocity structure of both black-hole driven and wind driven jets, namely the presence of helical vertical motion, a toroidal field structure at large distances that collimates the poloidal field near the black hole, and a jet-like velocity field that can evolve to a relativistic disk wind at large radii.

In covariant notation, using the electromagnetic field tensor $F^{\mu\nu}$ and the four-current j^{ν}, the force-free condition is expressed as

$$F^{\mu\nu} j_{\nu} = 0, \tag{1.4}$$

For an axisymmetric system, and recalling Maxwell's equations $\nabla_{\nu} F^{\mu\nu} = 4\pi j^{\mu}$, the force free condition can also be written as

$$F^{\mu}_{\nu} \nabla_{\sigma} F^{\nu\sigma} = 0, \quad \text{or} \quad \nabla_{\sigma} F^{\mu\sigma} = \alpha b^{\mu}_{F} + \xi u^{\mu}_{F}, \tag{1.5}$$

where b^{μ}_{F} and u^{μ}_{F} are the magnetic field and jet velocity four-vectors respectively.

The magnetic field structure is defined by quasi-parabolic field lines near the black hole, described by the stream function

$$\psi = r^{2-2\xi}(1 - \cos\theta), \tag{1.6}$$

where r is the radius, θ is the polar angle, and ξ is a constant related to the jet collimation rate. At $\xi = 0$ the jet is cylindrical, and at $\xi = 1$ the jet is conical, with intermediate values producing parabolic jets. This stream function is also dependent on the angular velocity Ω of the jet at the equator, and the associated jet velocity is $u^{\mu}_{F} = u^{t}_{F}(1, 0, 0, \Omega)$. Outside the inner-most stable circular orbit (ISCO), the angular velocity is the Keplerian angular velocity, and fixed to the ISCO value inside. The field line that connects to the ISCO is a surface that exhibits the largest accelerations and highest Lorentz factors, and serves as a convenient boundary for what determines the jet. The perpendicular distance from the black hole to this surface we call ρ_{crit}, and is used throughout this paper as an important reference position when initializing our simulations. This form of the stream function is an approximate solution to a second order partial-differential equation, and is within 10% of the true stream function inferred from non-relativistic numerical simulations (Tchekhovskoy et al., 2008).

The poloidal magnetic field structure can then be expressed in the jet frame as

$$b^{r}_{F} = -B_0 \frac{\sigma r^{2-2\xi} \sin\theta}{u^{t}_{F}\sqrt{-g}}, \text{ and} \tag{1.7}$$

$$b^{\theta}_{F} = B_0 (2 - 2\xi) \frac{\sigma r^{1-2\xi}(1 - \cos\theta)}{u^{t}_{F}\sqrt{-g}}, \tag{1.8}$$

where $\sigma = u_F^\mu u_{F\mu} = \pm 1$. At large distances, the poloidal field dominates (Tchekhovskoy et al., 2008), so we can write the toroidal magnetic field as just a function of ψ,

$$b_F^\phi = -2B_0 \Omega \psi u_F^t. \tag{1.9}$$

Then, since since $u_F^\mu b_{F\mu} = 0$, the temporal component of the magnetic field must be $b_F^t = -\Omega b_F^\phi$.

To illuminate the force-free jet model, we use a radial Gaussian electron distribution dependent on the Lorentz factor in the jet at large distances, and on the size of the jet footprint at the mass-loading height. For a low mass-loading height, the jet will produce a bright crescent-like ring around the black hole shadow, with limited emission further from the shadow. These simulated images can then be directly compared to images and data produced by the Event Horizon Telescope (EHT), which should allow us to investigate the jet-launching region and place constraints on the jet launching mechanism.

1.4 Event Horizon Telescope

The EHT is a global millimetre-wavelength, very-long baseline interferometer (mm-VLBI), capable of generating the first images of an AGN and resolving the horizons of the central supermassive black holes (Event Horizon Telescope Collaboration et al., 2019a,b,c,d,e,f). Currently, the EHT is comprised of eight telescopes located at six sites: the Submillimeter Array (SMA) and James Clerk Maxwell Telescope (JCMT) in Hawaii, the Arizona Radio Observatory Submillimeter Telescope (ARO-SMT) on Mt. Graham, the Large Millimeter Telescope (LMT) in Mexico, the Atacama Large Millimeter/Submillimeter Array (ALMA) and Atacama Pathfinder Experiment (APEX) in Chile, and the Institut de Radioastronomie Millimetrique 30m Telescope in Pico Veleta (PV). While unable to observe M87 due to the latitude, the South Pole Telescope (EHT) was involved in the observations of Sgr A* and some calibrator sources. Together, these present Earth-sized baselines to the primary EHT targets, Sgr A* and M87.

In April of 2017, the EHT successfully observed the black hole at the center of M87, and produced the first horizon-scale images of a black hole and its immediate surroundings. At a distance of 16.8 Mpc, the angular diameter of M87 is 42 μas, and appears as an asymmetric ring with a deep central depression. Since the angular diameter of the black hole shadow is directly proportional to the black hole mass, and thus angular size, one can estimate the mass of a black hole by measuring the angular diameter of the black hole shadow projected onto its surrounding material. However, the turbulent material providing the emission

source can also complicate a direct estimate of the shadow diameter due optical depth and resolution effects.

To make a precise mass estimate, there was an extensive effort to calibrate the angular gravitational radius measurement on simulated observations of hundreds of GRMHD simulations (Event Horizon Telescope Collaboration et al., 2019e,f). After this calibration procedure, the angular diameter corresponds to a mass of $6.5 \times 10^9 M_\odot$, consistent with the mass estimate from a previous stellar dynamics study (Gebhardt et al., 2011). The flux asymmetry in the image is suggestive of significant angular momentum, and the axis of angular momentum implied by the asymmetry is consistent with the jet axis at lower frequencies and larger scales (Event Horizon Telescope Collaboration et al., 2019d,e,f).

The EHT and the images it produces are the best tools we have to investigate the jet-launching region of AGN. With the images of M87* in hand, it is now possible to compare them against models of the accretion flow. So far, the existing EHT analysis has focused on GRMHD simulations (Event Horizon Telescope Collaboration et al., 2019e), that, while powerful, are limited to purely thermal emission and have difficulty describing regions with high magnetic energy density. GRMHD simulations are also computationally expensive, so in order to develop a wide range of simulated data, it may be better to use semi-analytical models, especially when we can use semi-analytical models to directly investigate different non-thermal emission mechanisms.

Chapter 2

Horizon Scale Jet Variablity

Simulated images from semi-analytic models differ from images generated from general relativistic magnetohydrodynamic (GRMHD) simulations primarily through the distributions of the synchrotron emitting lepton populations. While the magnetic field and energy density are well described in GRMHD simulations, the particle content in regions of high magnetic density is not well recovered (Dexter et al., 2012). Non-thermal particle emission in the highly magnetized regions could arise from turbulence or magnetic reconnection events well below the simulation resolution, and efforts to produce a self-consistent model for the evolution of the non-thermal particle distribution are still underway (Mościbrodzka et al., 2016). Because of this, jet variability in these GRMHD simulations are strongly dependent on numerical noise in the jet-launching region and may not adequately model observed variability in M87. Indeed, when comparing GRMHD models to the observations of M87, the emissivity was set to zero in regions where the magnetization was order unity due to the unreliable nature of the emission (Event Horizon Telescope Collaboration et al., 2019e).

For simplicity, the force-free jet model used in this work is time-stationary, and we add variability by introducing compact emission regions within the jet-launching zone, but do not allow these compact regions to affect the field structure of the jet. As a result some intrinsic variability that is expected from the turbulent accretion flow and jet is not captured by the semi-analytic model, but we also do not impose any restrictions on the particle emissivities in regions of high magnetization. Force-free jets are not generally time stationary, but this work serves as a pilot study to explore the effects of hot-spot variability in the jet launching region as a way to distinguish black hole driven and wind-driven jets. While outside the scope of this work, one could physically motivate these spots as reconnection products at the jet boundary, particle creation events inside the jet,

or as wind material blown up from the accretion disk. These "spots" are similar to those employed within the accretion flow environments in Broderick & Loeb (2006b), with two key exceptions: 1. following injection they subsequently outflow along the highly-stratified velocity field of the stationary force-free jet model, and 2. they necessarily shear. We find that both the small- and large-scale features of the 1.3 mm images are strongly dependent on the initial spot injection location. Thus, the nature and properties of the variability in EHT observations of M87 is diagnostic of the location of the jet launching region and the origin of the emitting jet leptons.

The radio wavelength images of M87 made by Ly et al. (2007); Mertens et al. (2016a); Hada et al. (2016), among others, show clear evidence of structure in the jet at lower frequencies. While this work does not seek to explain the physical mechanisms of generating these structures, we do want to explore how the EHT might see jet structure near the black hole. To this end, we model these structures, or spots, as an over-density of non-thermal electrons which we construct to initially have a spherical Gaussian distribution in the reference frame of the spot center. The physical motivation for these spots is that a high energy event occurs near the base of the jet near the black hole, generating a large population of non-thermal particles. The jet is overwhelmingly dominated by Poynting flux this close to the black hole Tchekhovskoy et al. (2008); McKinney et al. (2012), so large fluctuations in the emissivity should not significantly alter the larger jet structure. The motion of the spot is determined solely by the location of the spot center, which follows a single stream line up the jet, and the density profile of the spot stays fixed to the spot center.

Our jet model produces a velocity field that accelerates particles up the jet, but also includes significant shearing in the azimuthal plane. In Figure 2.1, we show the velocity (blue) and magnetic (green) field structures. In our jet model, we fix the angular velocity Ω inside the critical surface (red dashed line) to the value at the critical surface, as described in Broderick & Loeb (2009). In many simulations, Ω is generally smaller than the angular velocity at the ISCO, as in McKinney et al. (2012). To investigate the effects of reduced Ω on the velocity field, we artificially extended the jet inner radius away from the ISCO (orange dashed line). This serves to decrease Ω inside the critical surface. As shown in Figure 2.1, increasing the jet inner edge reduces the angular velocity (blue contours) inside the critical surface, and produces a shallower Ω gradient across the cylindrical radius. Outside the critical surface, Ω is unchanged. Thus, reducing Ω inside the critical surface should have no effect on hotspots launched outside the critical surface, and will only affect the evolution of spots launched inside the critical surface. Regardless, extended emission regions still become distorted and sheared out, changing the emission profile dramatically depending on where in the velocity field the spot is launched. A spot with a fixed density

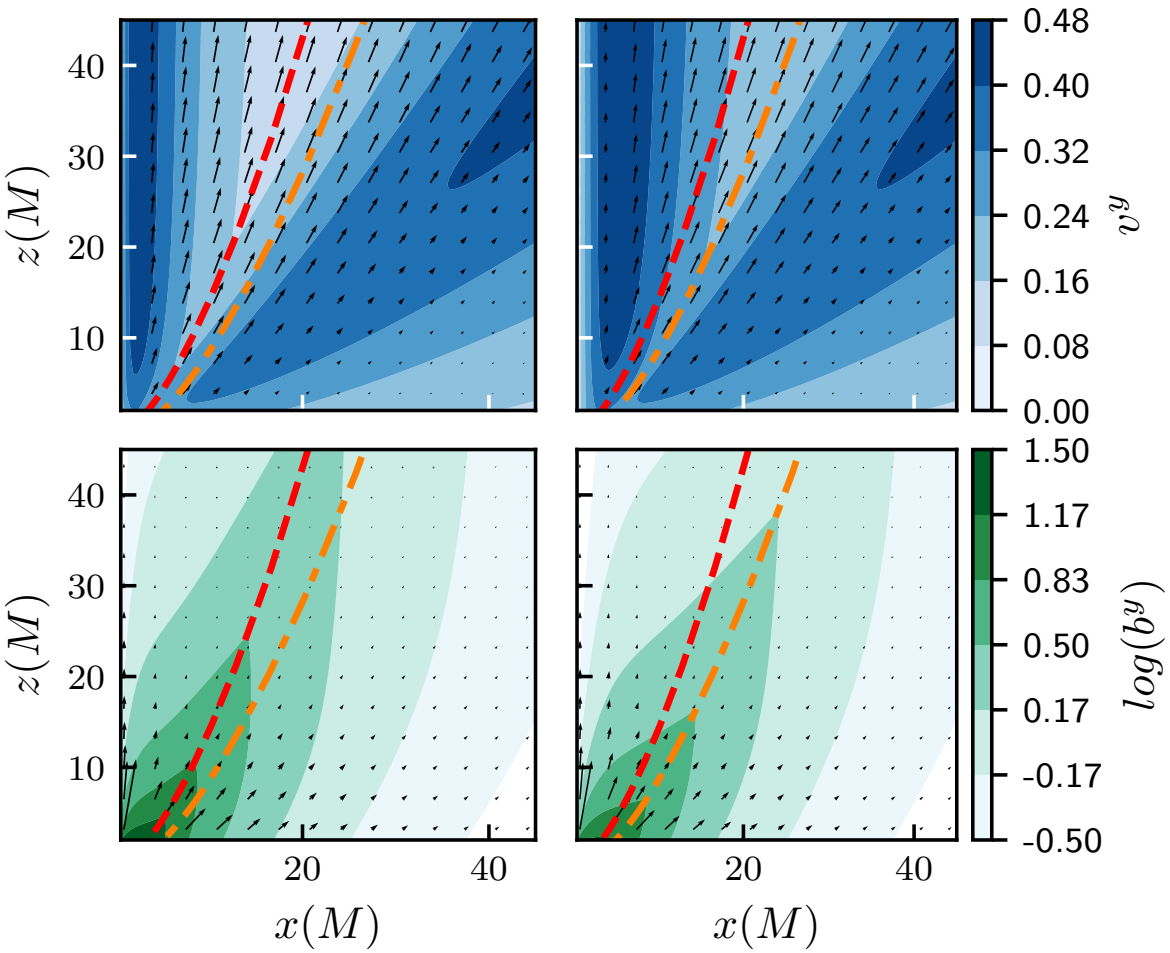

Figure 2.1: Velocity (blue) and Magnetic (green) fields of the jet in the x-z plane. The vector field shows the magnitude and direction of the x and z (poloidal) components, and the contours show the magnitude of the y (toroidal) component, where darker contours correspond to higher values. As we travel up the jet, the magnitude of the toroidal velocity component (v_y in this slice) drops, while the poloidal velocity component (v_x and v_z) increases. The dashed curves represent the streamline connected to the inner jet edge. The red dashed curve is the streamline for an inner jet edge at the ISCO, and the orange dashed curve is the streamline for an inner jet edge at 2 r_{ISCO}.

profile will not be able to adequately simulate expected variability in our jet velocity field, so we must develop a method that allows the spot to shear out while maintaining a good approximation of the initial density profile of our non-shearing spot.

Throughout this chapter we specify distances in $M \equiv GM/c^2 = 1.0 \times 10^{15}$ cm and time in $t_g \equiv GM/c^3 \approx 9$ hr. Where appropriate, values in other units will be provided for convenience. In all models, the black hole has a dimensionless spin of $a \equiv J/M = 0.993$, where J is the spacetime angular momentum. While the M87 images and model comparisons produced by the EHT were not able to constrain the spin of M87, the jet power at larger scales and other frequencies are difficult to reproduce in GRMHD simulations with low spin (Event Horizon Telescope Collaboration et al., 2019e). All images are simulated observations at 1.3 mm, and show a logarithmic intensity scale over four orders of magnitude, normalized so that the total image intensity of just the quiescent jet without a spot is about 0.7 Jy.

2.1 Construction of Shearing Spots

While our Gaussian spots should adequately model the general motion of over-densities in the jet, the shearing forces near the black hole non-trivially affect the structure of these spots as they evolve. In order to confidently explore the impact of this type of jet variability on EHT images, we need to think carefully about how to initially construct and keep track of the changing spot. We construct a shearing spot as an assembly of smaller non-shearing spots arranged in equal mass shells that approximate the density structure of the non-shearing spot. These mini-spots serve as Lagrangian control points for calculating the local density in a way similar to smoothed particle hydrodynamics methods.

To be able to propagate the mini-spots through the jet velocity field, we need a set of coordinates ξ that co-move with each mini-spot.

$$\xi_1^\mu = \epsilon^{\mu\alpha\beta\gamma} t_\alpha z_\beta u_\gamma \tag{2.1}$$
$$\xi_2^\mu = \epsilon^{\mu\alpha\beta\gamma} t_\alpha \xi_{1\beta} u_\gamma \tag{2.2}$$
$$\xi_3^\mu = \epsilon^{\mu\alpha\beta\gamma} \xi_{1\alpha} \xi_{2\beta} u_\gamma, \tag{2.3}$$

where $\epsilon^{\mu\alpha\beta\gamma}$ is the 4th-dimensional Levi-Civita symbol, t_α is the lab frame time-like Killing vector, z_β is the lab frame vertical spatial unit vector, and u_γ is the lab frame velocity. Once these ξ are normalized, they serve as a space-like orthonormal triad that is also orthogonal to the lab frame velocity; together they form a complete spacetime basis.

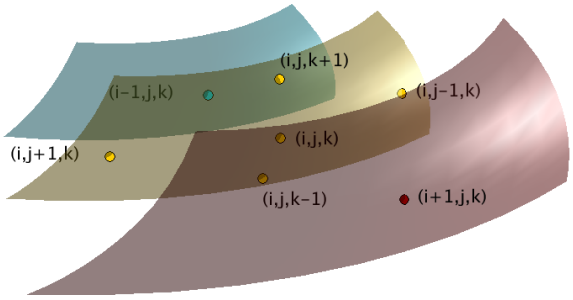

Figure 2.2: Sections from the outermost radial mini-spot shells showing central mini-spot (i, j, k) and its nearest neighbors in the cardinal shell directions. The mini-spots have been interpolated $5t_g$ from their initial launch time, and significant shearing from square in the θ and ϕ directions are apparent.

We divide our non-shearing density profile into radial, azimuthal, and polar shells evenly distributed by mass. From our co-moving cartesian basis we then construct the initial mini-spot distribution in Boyer-Lindquist coordinates x^μ_{ijk} where each i, j, and k index corresponds to a single mini-spot shell.

$$\begin{aligned} x^\mu_{ijk} = \rho_i \sin(\vartheta_j)\cos(\varphi_k)\xi^\mu_1 + \rho_i \sin(\vartheta_j)\sin(\varphi_k)\xi^\mu_2 \\ + \rho_i \cos(\vartheta_j)\xi^\mu_3 + r^\mu, \end{aligned} \tag{2.4}$$

where ρ, ϑ and φ are the shell indices for each mini-spot, and r^μ is the initial spot center position in the lab frame. Every mini-spot appears simultaneously in the frame co-moving with the spot center, but will appear at different Boyer-Lindquist times in the lab frame.

To find the mini-spot positions at later times, we calculate each mini-spot trajectory dx^μ_{ijk}/dt using the value of the velocity field u^μ_{ijk} at the mini-spot,

$$\frac{dx^\mu_{ijk}}{dt} = \frac{u^\mu_{ijk}}{u^0_{ijk}}. \tag{2.5}$$

We use a 4th/5th order Cash-Karp Runge-Kutta method to integrate along these trajectories, with adaptive step sizes determined by the error of the 4th order calculation Press et al. (2007). We first integrate backwards from our initial Boyer-Lindquist time to make sure we have mini-spot trajectories for every mini-spot in the lab frame, then integrate forward along the trajectories from the initial time to far enough in the future to travel

Figure 2.3: Density evolution of a non-shearing and shearing spot launched at $\rho = 0.5\rho_{\text{crit}}$ and $\phi = 270°$ for $30t_g$ in gravitational time. The top set of spots are a non-shearing spot with a Gaussian density profile in the spot-center reference frame, and the bottom set of spots are a shearing spot with the same initial launch position and density profile. The shearing spot develops an extended tail within a few t_g of launch, producing a very different density profile than the non-shearing spot.

significantly up the jet. We smoothly propagate each control point along their own streamline in the jet velocity field to create a spot path, which we tabulate at each integration step.

We can calculate the density at any point by adding up the density contribution from all the mini-spots nearby:

$$n_s = \frac{\rho_0 r_s^3}{N_s} \sum_j \frac{\exp\left(-\frac{1}{2}\Delta r_j I_j^{-1} \Delta r_j\right)}{\sqrt{|I_j^{-1}|}}. \tag{2.6}$$

Our total density n_s is made up of j mini-spots with individual number densities normalized by the correlated distance between one mini-spot and its nearest neighbors. Here, ρ_0 is the number density for an equivalently sized non-shearing spot, r_s and N_s are the spot radius and total number of mini-spots respectively, and Δr_j is the distance from where we want to calculate the density, at (r, θ, ϕ), to the mini-spot position x^μ_{ijk}. We add up the density contributions from each mini-spot by using an inverse covariance matrix I of mini-spot

positions, which lets us calculate the local density in the mini-spot coordinate frame:

$$I_{rr} = \sum_{[i'j'k']} \left(r_{i'j'k'} - r_{ijk}\right)^2 \tag{2.7}$$

$$I_{\theta\theta} = \sum_{[i'j'k']} \left(\theta_{i'j'k'} - \theta_{ijk}\right)^2 \tag{2.8}$$

$$I_{\phi\phi} = \sum_{[i'j'k']} \left(BC\left(\phi_{i'j'k'} - \phi_{ijk}\right)\right)^2 \tag{2.9}$$

$$I_{r\phi} = \sum_{[i'j'k']} \left(r_{i'j'k'} - r_{ijk}\right)\left(BC\left(\phi_{i'j'k'} - \phi_{ijk}\right)\right). \tag{2.10}$$

The sums in Equations (2.7 – 2.10) are over the mini-spot nearest neighbors to the central (i, j, k) location (in spot coordinates) where we want to calculate the density. The nearest neighbor spots are relative to their shell coordinates; the nearest r neighbors live in the $i+1$ and $i-1$ shells, the nearest ϕ neighbors live in the $j+1$ and $j-1$ shells, and the nearest θ neighbors live in the $k+1$ and $k-1$ shells. The BC function is a branch cut function that makes sure we calculate the shortest distance between two ϕ shells, to make sure that mini-spots at $\phi = 355°$ and $\phi = 5°$ are properly separated by . We only consider the covariance of nearest neighbors in the $r-r$, $\phi-\phi$, $\theta-\theta$, and $r-\theta$ directions because we do not expect much shearing in the $\theta-\phi$ or $r-\phi$ directions. Indeed, it is apparent in Figure 2.2 that this is the case, with the most significant shearing occurs in the radial and poloidal directions. Finally, the proper density is given by n_s/u^t.

Black hole driven spots should have a much more extended density profile than a non-shearing Gaussian spot launched with the same initial conditions. This is apparent in Figure 2.3, which shows the shearing spot with an extended tail feature forward of the spot central density, and a much more extended density region in general. Shearing spots launched at different launch radii should also develop different density profiles, demonstrated in Figure 2.4, since the velocity field structure changes significantly outside the critical field surface.

Even though spots might only differ in initial radial launch distance by less than $5r_g$ they exhibit substantially different density profiles after even a few gravitational time steps. A black hole driven spot will experience a much stronger velocity gradient than a wind-driven spot, and should be distinguishable in much the same way a non-shearing Gaussian spot is distinguishable from a shearing spot. Even though our jet model is relatively simple compared to GRMHD simulations, the techniques used to generate and track hotspots spots can be used in other jet models with more complicated velocity fields.

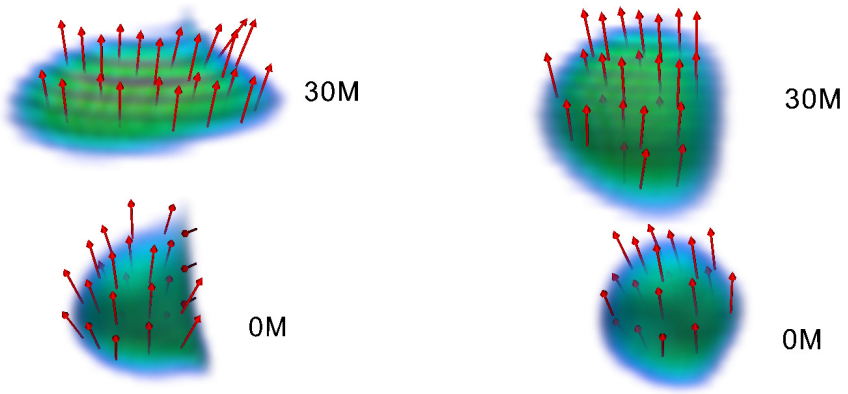

Figure 2.4: Density and velocity profiles for the spot launched at $\rho = 0.75\rho_{\rm crit}$ (left) and $1.25\rho_{\rm crit}$ (right) at $t = 0t_g$ (bottom) and $30t_g$ (top). The velocity profile for the outer spot (bottom two blobs) exhibits much less shearing, resulting in a more spherically symmetric spot as it evolves than the interior spot.

In practical terms, the shearing spot is initialized in terms of cylindrical launch coordinates, centered on the black hole. Throughout the rest of this paper, we will reference the radial cylindrical coordinate ρ, not to be confused with the initial non-shearing spot density profile. This radial launch coordinate is parametrized in units relative to the cylindrical radius of the critical field line or surface, which we denote as ρ_{crit}. Additionally, we can initialize the spot at different azimuthal positions around the black hole, which we denote with ϕ. With respect for the line of sight, a spot launched in front of the jet axis is initialized with $\phi = 0°$, and a spot launched behind the jet axis is initialized with $\phi = 180°$. This should also not be confused with the inclination of the jet, which is fixed in our simulations to be $i = 17°$, consistent with the results from Mertens et al. (2016b). The vertical position can also be specified, but is set to be $z = 3M$ for most of the simulations described in this paper. We discuss modifications to the launch height below.

2.2 Simulated Imaging of Shearing Spots

The primary emission mechanism near the black hole is synchrotron radiation from thermal and non-thermal electrons. The thermal component is modeled using the emissivity described in Yuan et al. (2003), and corrected to be fully covariant following the description

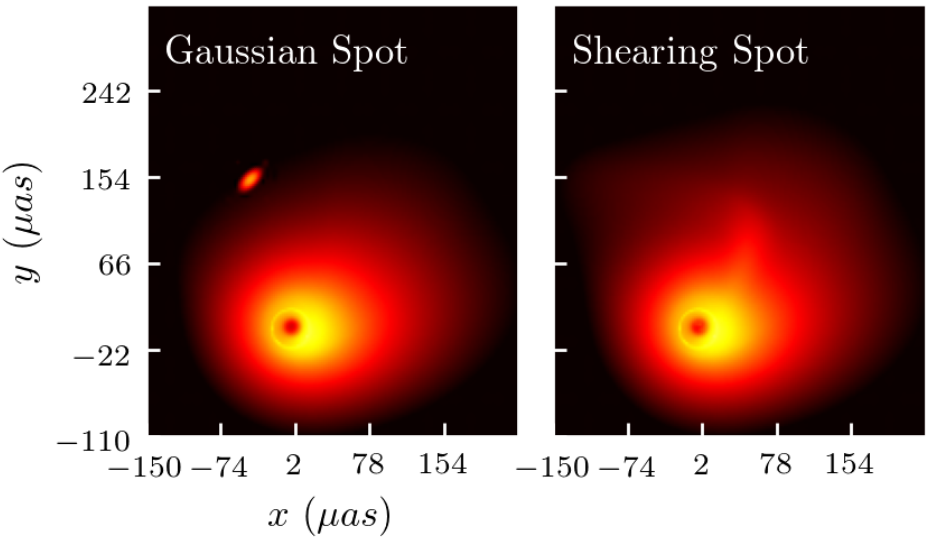

Figure 2.5: Snapshots at late times ($35t_g$) of a Gaussian and Shearing spot launched at $\rho = 0.5\rho_{\rm crit}$ and $\phi = 270°$. The non-shearing spot stays compact and bright, but the shearing spot develops complicated emission structures in the image plane, due to a combination of light delays and more spatially extended emission.

of covariant radiative transfer by Broderick & Blandford (2004). We assume the distribution of thermal electrons is isotropic, and use a thermal synchrotron polarization fraction derived in Petrosian & McTiernan (1983).

The non-thermal emission is assumed to follow a power-law distribution with an index of 1.19, and has a low frequency cut off below a critical Lorentz factor (Jones & Odell, 1977). The cut-off ($\Gamma_{min} = 100$) is fit to match M87's observed milimeter spectrum (Broderick & Loeb, 2009), and the absorption coefficients are determined directly from Kirchoff's law (Broderick & Blandford, 2004). Since most of the thermal emission comes from the accretion disk, and the accretion disk component is subdominant at 230 GHz (Broderick & Loeb, 2009), the images below only show contributions from the non-thermal jet.

The radiative transfer is performed by integrating the polarized photon distribution functions along null geodesics, or rays, sent back from the image plane, using the same code initially described in Broderick & Blandford (2004), and utilized in Broderick & Loeb

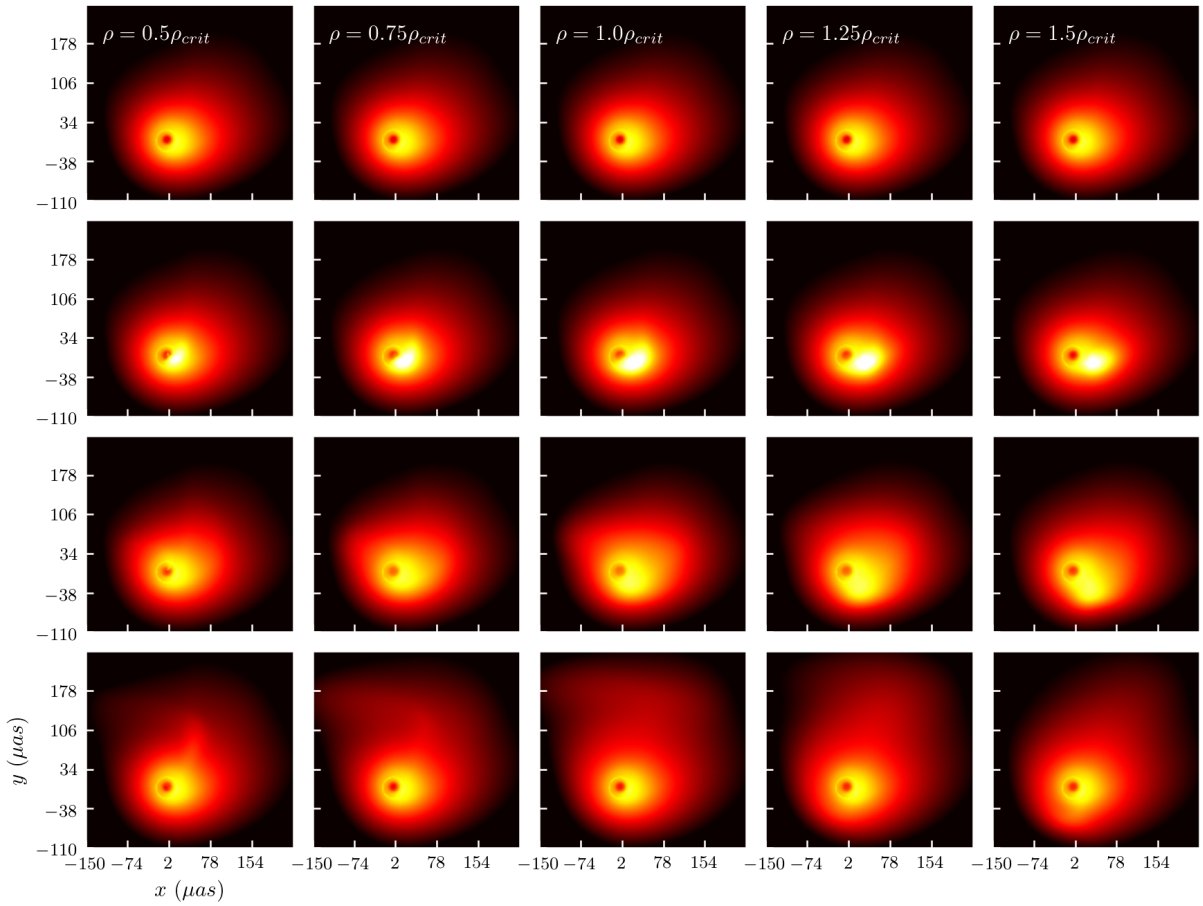

Figure 2.6: Snapshots of a shearing spot launched at different cylindrical positions, both inside and outside of the jet, showing evolution over time. From left to right, the columns correspond to spots with initial cylindrical radii at $0.5\rho_{\rm crit}$, $0.75\rho_{\rm crit}$, $\rho_{\rm crit}$, $1.25\rho_{\rm crit}$, and $1.5\rho_{\rm crit}$. In all cases the azimuthal launch location was $\phi = 270°$. Time flows from the top row to the bottom row, where between each row the observer time advances by $10t_g$ (90 hr). Spots launched inside the critical surface exhibit more complex emission structures when compared to spots launched outside the critical surface.

(2005, 2006a,b, 2009). The null geodesics are generated by integrating the pair of equations

$$\frac{dx^\mu}{d\lambda} = f(r)k^\mu \quad \text{and} \quad \frac{dk_\mu}{d\lambda} = -f(r)\left(\frac{\partial k^\nu k_\nu}{2\partial x^\mu}\right)_{k_\alpha}, \tag{2.11}$$

where the partial differentiation is taken while holding the covariant components of the wave four-vector k_μ constant, and λ is the affine parameter of the curve. The function $f(r) = r^2\sqrt{1 - r_h/r}$ (r_h is the radius of the horizon) is chosen to regularize the affine parameter, and make sure the ray avoids singularities at the horizon.

We integrate the photon distributions $\mathbf{N}_\nu = (N_\nu, N_\nu^Q, N_\nu^U, N_\nu^V)$ along the rays, where $N_\nu \propto I_\nu/\nu^3$ is the standard covariant intensity distribution, and the other components are the covariant analogues to the standard Stokes parameters as described in Broderick & Blandford (2004). Numerically, the radiative transfer is done by launching a set of initially parallel rays back through time from an image screen some large distance from the black hole, and then the photon distributions are integrated up along the rays forward in time to deposit back on the screen. Throughout this process, the speed of light is finite, and the emission properties can change in the time it takes the ray to travel back to the screen. This is in contrast with the radiative transfer done in most GRMHD simulations, where the GRMHD state is essentially held constant throughout the ray propagation time, meaning an effectively infinite speed of light (Gold et al., 2020). The "slow-light" method used in this work can thus accurately model time-delay effects from rapidly variable emission processes.

2.3 Exploration of Launch Position

The distributed density profile of the shearing spots is easily distinguishable from the Gaussian spot not only in local density profiles but also in the image space. Figure 2.5 shows a snapshot at $35t_g$ (about 315 hours or 13 days) after the initial launch, and the shearing spot exhibits a much more extended intensity profile, compared to the small, compact non-shearing Gaussian spot. The shearing spot has progressed up the jet long enough to wrap up on itself at least once, creating a distinct arc over the bright jet emission near the black hole.

We have demonstrated that the shearing spot is substantially different from the Gaussian spot in both its density profile and in the image domain. Our next task is to compare shearing spots at different launch positions. The M87 model used in this paper has a large spin, $a = 0.993$, resulting in a strong velocity field very close to the black hole. This means

photons from our spots can be strongly beamed towards or away from us when the spot is near the black hole, in addition to beaming associated with the acceleration from the jet itself. The geometry of the velocity field near the jet will also lead to different shearing morphologies, depending on whether the spot was launched inside or outside the jet critical surface.

Zooming into the immediate region around the black hole at early times, we can still see differences in image structure when we change the spot launch radius. Even though the spot is very bright at early times, we can see in the top two rows of Figure 2.6 that black hole-driven spots shear away faster than wind-driven spots. We can also see how spots starting at the critical radius initially look very much like black hole-driven spots, but shear into structures similar to wind-driven spots at later times.

Spot densities for wind-driven spots remain relatively compact, as seen above in Figure 2.4. Even after $30t_g$ (11 days), wind-driven spots are only slightly more extended compared to their launch size. Nevertheless, propagation time delays smear the spots on the image plane. While this happens for black hole-driven spots as well, this phenomenon is easiest to see in wind-driven spots, where the spot both shears and travels much more slowly.

If we zoom out and look at the spot for longer, as we do in the bottom two rows of Figure 2.6, the same conclusions still apply: azimuthal shearing is most significant inside the critical surface (about $4r_g$ for a launch height of $3r_g$), which is responsible for low surface brightness arcs. Outside the critical surface, azimuthal shearing is significantly suppressed, and the spot slowly expands and flows outward, generating an extended arm in the last column.

Figure 2.6 demonstrates that spots launched inside the jet critical surface exhibit sheared structures that distinguish them from spots launched outside the critical surface. The spot launched at $\rho = 0.5\rho_{\rm crit}$ (first column) looks much different than the spot launched at $\rho = 1.5\rho_{\rm crit}$ (last column). The black hole-driven spot creates a thin arc in the last row, $35t_g$ (13 days) after the spot was launched. The spot arc is still present for the spot launched on the critical surface, whereas the exterior spots have a more extended emission region coming straight out of the bright jet region. Spots launched outside the critical surface exhibit much dimmer arcs, and perpendicular structures disappear entirely for spots launched only $2r_g$ ($\rho = 1.5\rho_{\rm crit}$) away from the critical surface.

Without a spot, the jet electron density is set such that the total intensity for a quiescent jet is approximately 0.7 Jy, which is consistent with the measurements of compact flux from geometric model fits in Event Horizon Telescope Collaboration et al. (2019f). For a fixed spot electron density, the maximum intensity in the image depends strongly on the initial radial launch position. The spot appears brightest when launched on the critical

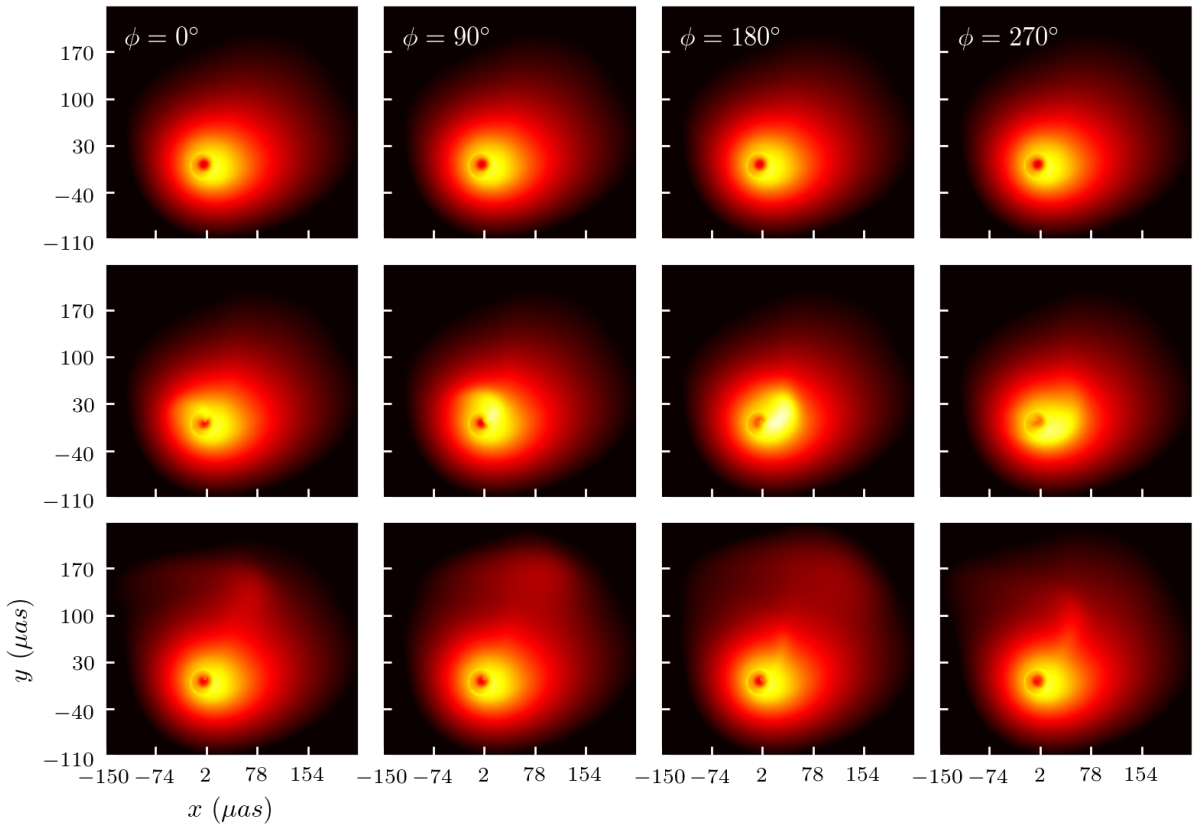

Figure 2.7: Images of a shearing spot at $\rho = 0.5\rho_{\rm crit}$ at cylindrical angles ϕ of 0°, 90°, 180° and 270° showing early evolution. Time flows from the bottom row to the top in steps of $15t_g$ (5 days), starting $5t_g$ after the spot is launched. Changing the launch azimuthal position dramatically changes the spot intensity and location of extended structure in the image.

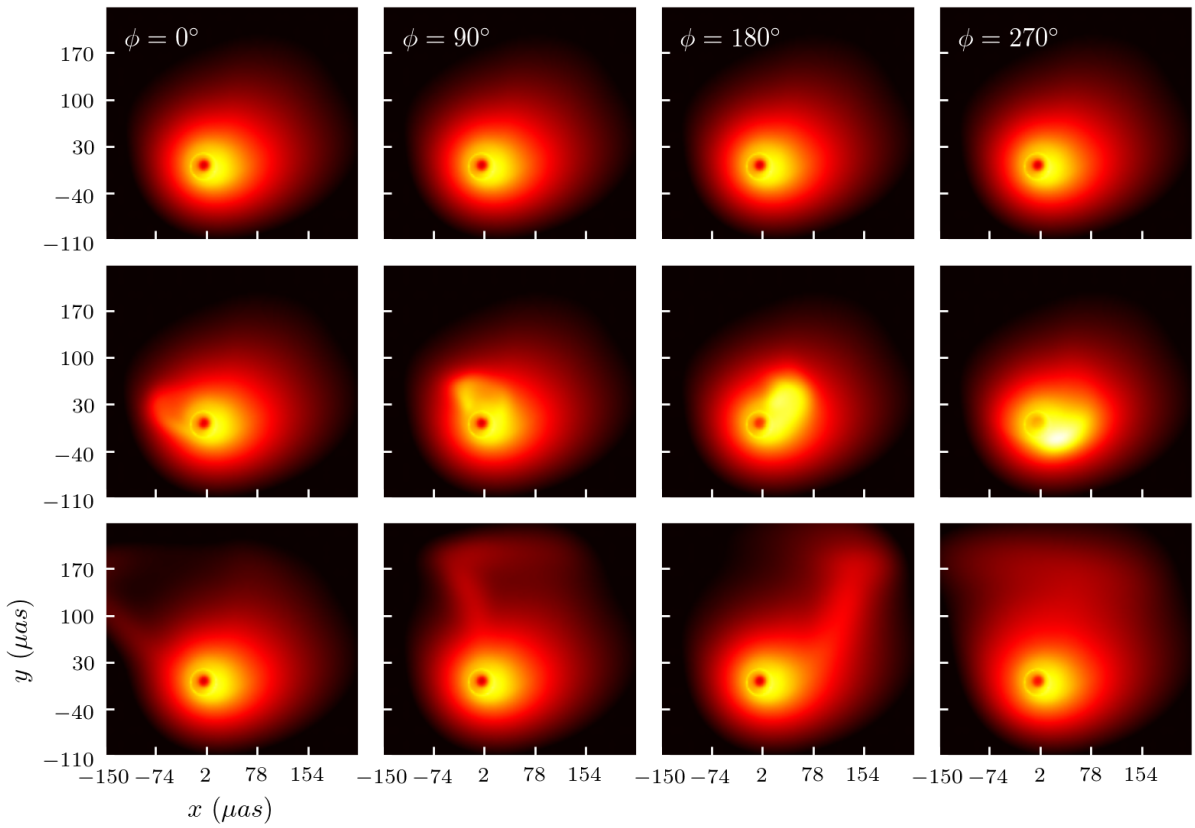

Figure 2.8: Images of a spot launched at $\rho = 1.0\rho_{\text{crit}}$ with ϕ angles of 0°, 90°, 180°, and 270° showing early evolution. The top row is $5t_g$ (45 hours) after the spot launch, the second row is $20t_g$ (7.5 days) after the spot launch, and the bottom row is $35t_g$ (13 days) after the spot launch. Changing the azimuthal launch parameter produces significant differences in image intensity, with spots launched at low angles contributing to a much lower image intensity than spots launched at large angles. Complicated arc structures away from the black hole are evident at late times.

surface, and falls off faster when launched inside the jet. The shorter spot half-life for black hole driven spots can be attributed to stronger shearing compared to wind driven spots, which serves to disrupt and dilute the spot intensity inside the jet. Spots outside the jet experience less shear, and remain relatively more compact for longer. A more in depth discussion about spot light curves is reserved for Section 2.4.

Fixing the radial launch position to 50% the critical surface but varying the azimuthal launch angle around the jet dramatically alters the structure of intensity in the image, especially at late times. These dramatic differences can be attributed to different projections of the shearing spot as it shears around the jet, and there is qualitatively no structural differences in the local spot density structure between these different launch positions. The spot in each of these cases shears in the same way and in the same amount of time, as we can see in Figure 2.7. At late enough times, e.g., the last row of Figure 2.7, there is a thin arc emerging from the edge of the black hole shadow towards the low surface brightness structures further away from the black hole. This region is the tail of the spot re-entering the region of the jet that provides the strongest beaming. Even though the spot tail has very low density, the beaming in this region of the jet is strong enough to make the tail of comparable brightness to the main spot arc.

Similar to black hole-driven spots, launching spots on the critical surface at different azimuthal positions leads to substantially different emission structures in the image at later times, as seen in Figure 2.8. Even so, these different structures are different projections of the same spot arc around the jet. Arcs in these images stay relatively compact and bright compared to arcs associated with black hole-driven spots. Spots on the critical surface shear less than spots inside the critical surface, and no spot on the critical surface shears completely around in the simulated time.

Also similar to black hole-driven spots, fixing the radial launch position to the critical surface but changing the azimuthal launch position changes the apparent brightness of the spot as it moves around the jet, as we can see in the second row of Figure 2.8. The spot launched on the side with the highest beaming, $\phi = 270°$, has a much higher brightness compared to the spot launched at $\phi = 0°$. The spot intensity half-life is approximately the same for spots launched on the critical surface as as spots launched inside the jet.

As mentioned earlier, the consequences of slow light can best be seen in images of wind-driven spots. We can see in Figure 2.9 that for intermediate times, e.g., in the second row, the image of the spot is relatively compact, and approximates the physical structure of the spot at different projections. At later times, the image of the spot stretches into an extended, diffuse arm even though the spot itself remains relatively spherical.

Wind-driven spots are generally dimmer relative to interior or critical spots, except on

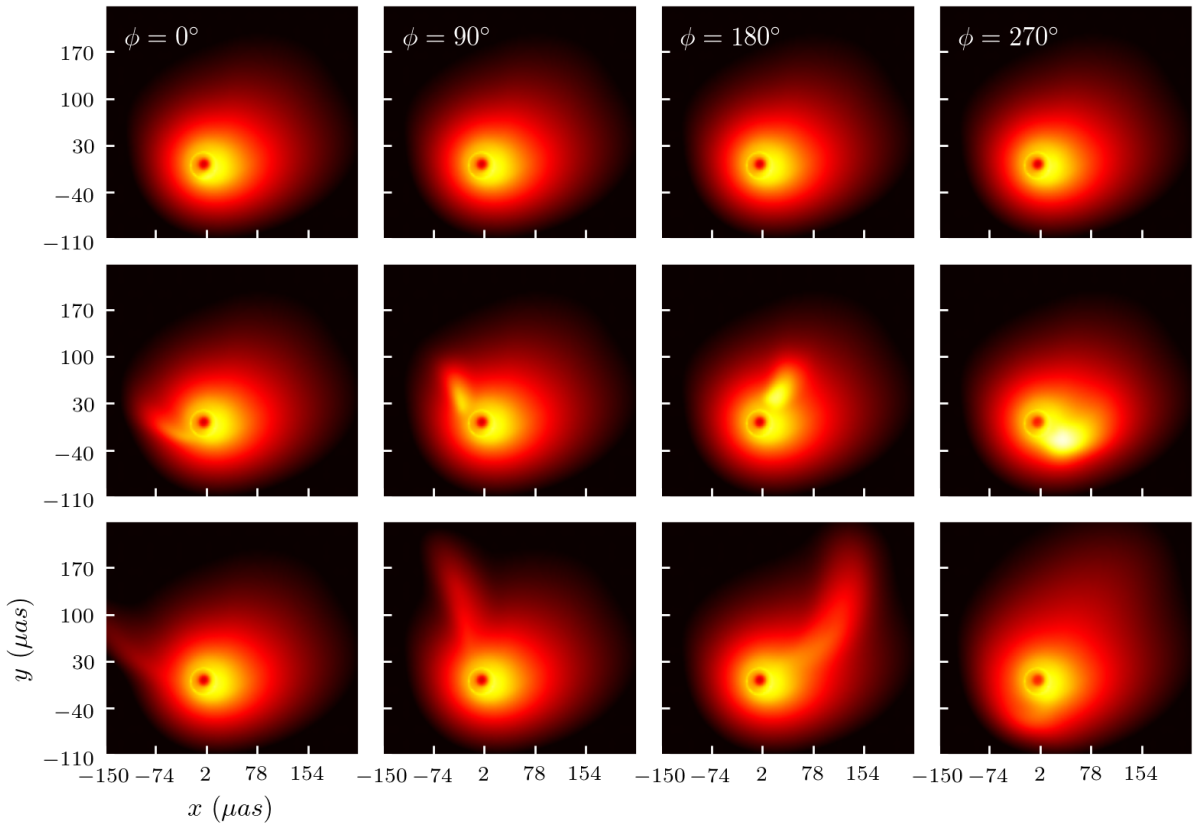

Figure 2.9: Horizon scale images of a spot launched at $\rho = 1.5\rho_{\rm crit}$ and at ϕ angles of 0°, 90°, 180°, and 270°. The top row is $5t_g$ (45 hours) after the spot launch, the second row is $20t_g$ (7.5 days) after the spot launch, and the bottom row is $35t_g$ (13 days) after the spot launch. The spot density remains compact and relatively spherical, and projection effects and light delays produce the dim extended arms at late times. The spot intensity is generally comparable to the underlying jet intensity.

the brightest side of the jet ($\phi = 270°$). While these spots may not be as bright as other spots, they contribute significantly to the overall image intensity for much longer.

Fixing the radial and azimuthal launch positions but altering the launch height is approximately degenerate with changing the observer time for the spot image. Spots that start at a higher position look structurally very similar to later images of spots launched at lower heights. For example, the spot launched at $12M$ and seen about 135 hr after launch looks very much like a spot launched at $6M$ imaged 225 hr after launch (Figure 2.10).

The time delay signature apparent in the images of spots launched at different heights are also visible in the light curves, as demonstrated in Figure 2.11. Spots launched at $h = 3M$ start contributing additional flux beyond the quiescent jet around $t = 10t_g$ after the spot launch, and spots launched at $h = 6M$ start brightening only a few t_g after the spot launch. This delay can be attributed to the shape of the velocity streamlines, which are roughly parabolic. Close to the black hole, the spot is accelerating up the jet perpendicular to the line of sight, but eventually travels mostly parallel to the line of sight. Since the intensity is strongly dependent on beaming effects, the spots only contribute to the image intensity when they are traveling parallel to the line of sight. For spots launched higher up the jet, e.g. at $h = 12M$,the spot immediately accelerates parallel to the line of sight.

2.4 Light Curves as Diagnostic

The total averaged image intensity is an easily accessible and measurable quantity that can be accessed without full image reconstructions of the horizon region. Here we discuss in more detail how the total image intensity changes with spot azimuthal launch position, and how changing the spot launch radius changes the image intensity decay time outside the jet.

To explore the effect of different azimuthal launch positions on the structure and maximum intensity in the light curves, we generated a shearing spot simulation every 20° around the black hole for spots launched at $\rho = 0.5,\ 1.0$, and $1.5\rho_{crit}$. For each simulation and associated light curve, the maximum image intensity is shown in Figure 2.12 as a function of azimuthal launch position, ϕ. The quiescent jet without a spot has a total image intensity of about $I = 0.7\ Jy$. The brightest spots are launched between $\phi = 210°$ and $\phi = 300°$, and peak around $\phi = 270°$ for spots launched on the critical surface, as shown by the orange dashed line in Figure 2.12. Wind driven spots are also brightest around $\phi = 270°$, but exhibit the lowest maximum intensities compared to other spots when launched between

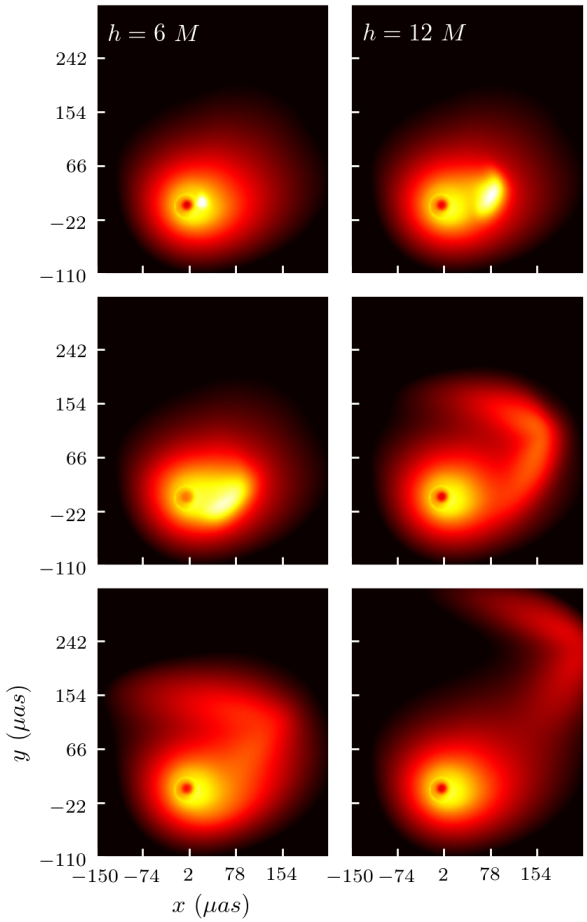

Figure 2.10: Altering the launch height of spots launched at $\rho = \rho_{\text{crit}}$. The first column is a spot launched with a height of $6M$ and the second column is a spot launched with a height of $12M$. The first row corresponds to $t = 5t_g$ (45 hours) after the spot launch, and the second and third row correspond to $t = 15t_g$ and $t = 25t_g$ respectively. Early time spots at high launch heights look qualitatively like late time spots with low launch heights.

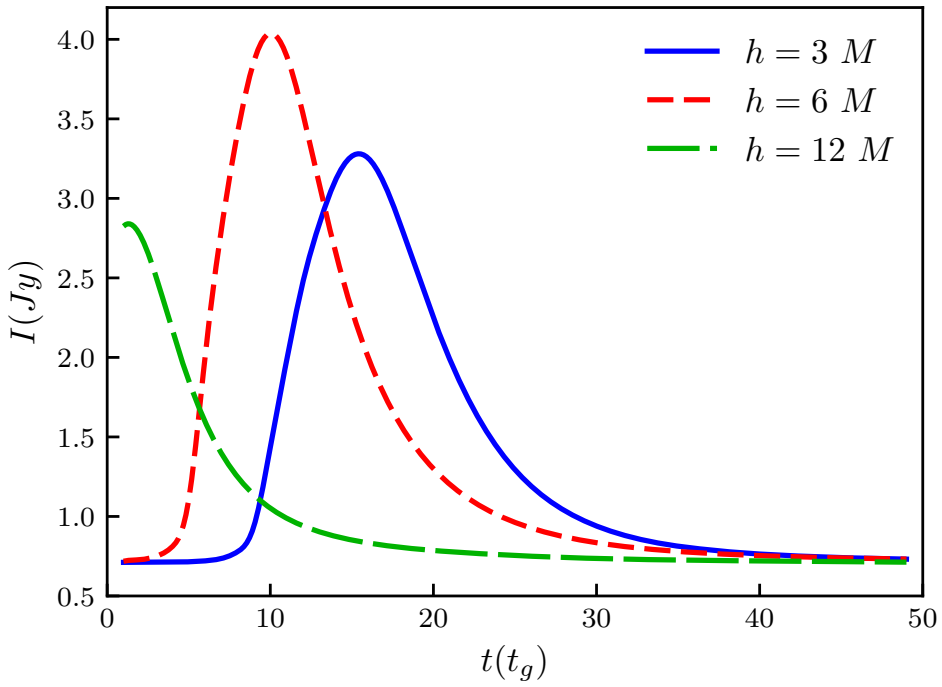

Figure 2.11: Light curves of a shearing spot launched at $1.0\rho_{\rm crit}$. The spot was launched at 270°, at heights of $h = 3M$ (blue solid), $h = 6M$ (red dashed), and $h = 12M$ (green long dashed). Spots that start lower than $6M$ experience a full rise, peak, and fall in their light curve.

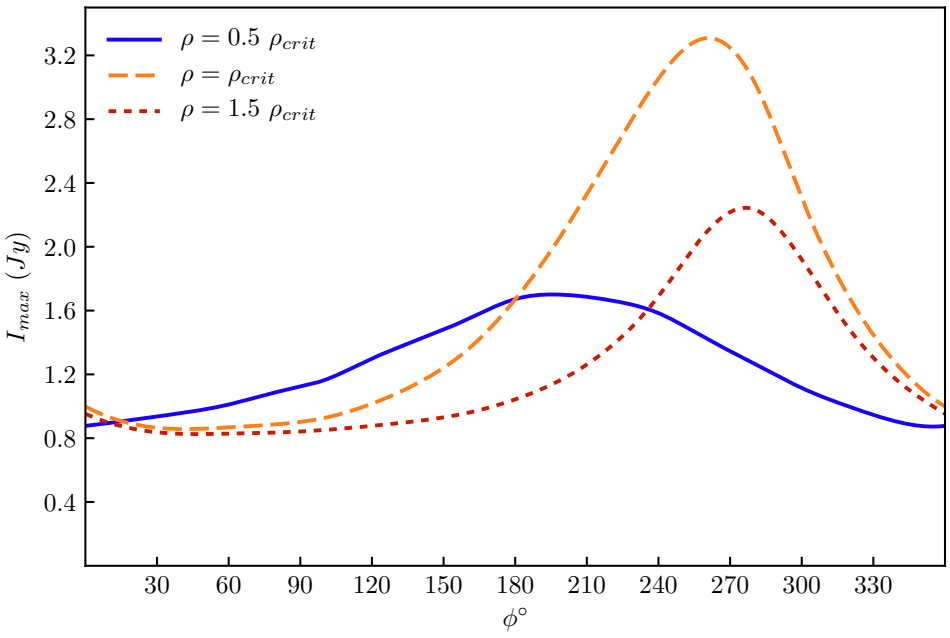

Figure 2.12: Maximum image intensity as function of azimuthal launch position ϕ for a spot launched at $\rho = 0.5\rho_{\rm crit}$ (blue solid line), $\rho_{\rm crit}$ (orange dashed line), and $1.5\rho_{\rm crit}$ (red dotted line). The maximum intensity peaks near $\phi = 270^{\circ}$ for wind driven spots and spots launched on the critical surface, but black hole driven spots have a shallower and broader maximum intensity distribution.

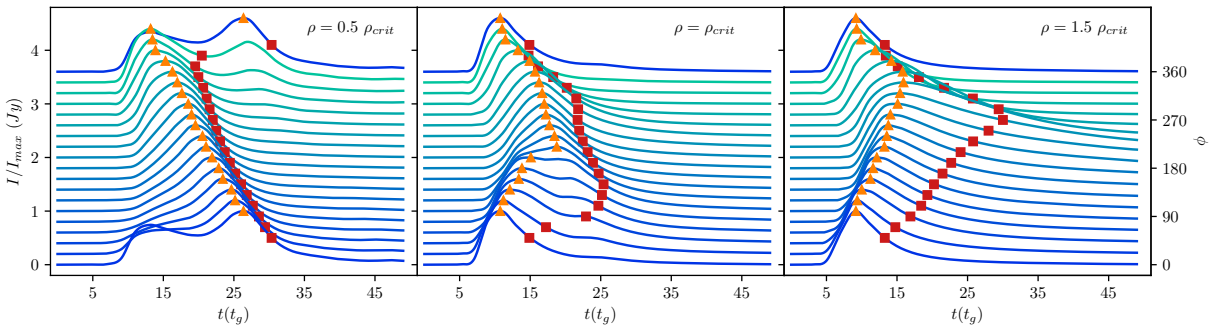

Figure 2.13: Normalized light curves as function of azimuthal launch position ϕ for spots launched at $\rho = 0.5\rho_{\rm crit}$, $\rho_{\rm crit}$, and $1.5\rho_{\rm crit}$. Successive light curves are shifted by a constant factor. The maximum intensity is denoted by an orange triangle, and the half-maximum intensity is denoted by a red square. Contributions to the light curve from secondary spot features produces non-trivial evolution in the maximum intensity and spot half-life for black hole driven spots. Light curve features evolve smoothly for wind driven spots.

$\phi = 10°$ and $\phi = 240°$. For black hole driven spots launched at $\rho = 0.5\rho_{crit}$, the brightest spots are launched closer to $\phi = 180°$, and only reach about half the peak intensity of spots launched on the critical surface.

The region of azimuthal parameter space where beaming boosts the image intensity to > 3 times the quiescent jet occurs between $\phi = 200°$ and $\phi = 300°$, about a quarter of the total azimuthal parameter space. Outside this region, the maximum intensity remains within a factor of 2 or less of the quiescent jet. Image reconstructions and geometric model fits to M87 presented in Event Horizon Telescope Collaboration et al. (2019d,f) were fit to visibility amplitudes, which allowed for some measurement of the compact flux in the EHT images. The average measurement was $0.66^{+0.16}_{-0.10}\ Jy$ for image domain measurements, and $0.75\ \pm 0.3\ Jy$ for geometric models, but the measurements may suggest a rise in flux during the first two observations and a fall over the last two observations.

Ideally, to identify and analyze these energetic events, the spot must persist long enough to be seen in at least two observations during the EHT observing window. The time it takes for a spot to evolve from its maximum intensity to half the maximum is a useful quantity for characterizing the spot lifecycle. For a spot starting on the critical radius, the spot half-life is largest when the spot starts on the dim side of the jet ($\phi \approx 120°$), as see in the centre panel of Figure 2.13. Here, the spot half-life is approximately 90 hr, but drops to around 45 hr when the spot should be brightest ($\phi = 270°$). This variation in spot

half-life can be attributed to the presence of secondary features in the light curve caused by the spot tails entering the strongly beamed region. This appears in all black hole driven spots, and produces breaks and discontinuities in the time of the max and half-maximum intensities. For a spot launched at $0.5\rho_{crit}$, this leads to a $10t_g$ jump between the maximum intensities between spots launched between $\phi = 340°$ and $\phi = 360°$.

Wind driven spots exhibit more gentle light curve evolution with azimuthal launch position. Both the maximum and half-maximum intensity smoothly rise to peak at $\phi = 270°$, and then fall back down to the original times at $\phi = 0°$. Wind driven spots also exhibit the longest half-lives, where a spot launched at $1.5\rho_{crit}$ has a half-life of about $15t_g$ when launched at $\phi = 240°$.

Within the context of the Event Horizon Telescope Collaboration et al. (2019f) compact flux measurements, the weak rise and fall over the 6 day observation period does not allow us to put constraints on our spot model at this time. Most of the uncertainty in the measured flux comes from systematic uncertainty in the calibration of the geometric models to a large library of GRMHD simulations. If future analyses or observations are able to restrict the allowed GRMHD simulations, and thus contract the systematic error in the flux calibration, then it may be possible to connect the variability at horizon scales to these shearing spot models, and either constrain or rule out certain regions of the spot parameter space.

At very low azimuthal launch angles ($\phi \approx 0°$), all spots have approximately the same maximum intensity and half-life. However, black hole driven spots may still be distinguishable from wind driven spots by the presence of multi-modal features in the light curves. When spots are launched at higher azimuthal angles, and especially for spots launched to maximize their intensity, Figure 2.14 shows that there is a general increasing trend in spot half-lives for increasing cylindrical launch radius. By using a combination of maximum intensity, spot half-life, and the presence or absence of secondary features in the light curve, it should be possible to distinguish black hole driven and wind driven shearing spots.

2.5 Discussion

The emission from compact spots near the base of M87's jet is strongly shaped by the velocity field of the jet. Material originating inside or on the jet velocity critical surface experience significant shear forces on timescales of a few days, which means consecutive days of EHT observation could observe this type of variability. These spots are sheared into complex arcs perpendicular to the jet axis that are readily apparent in simulated reconstructed images of the black hole region of M87, and could be verified in the reconstructed

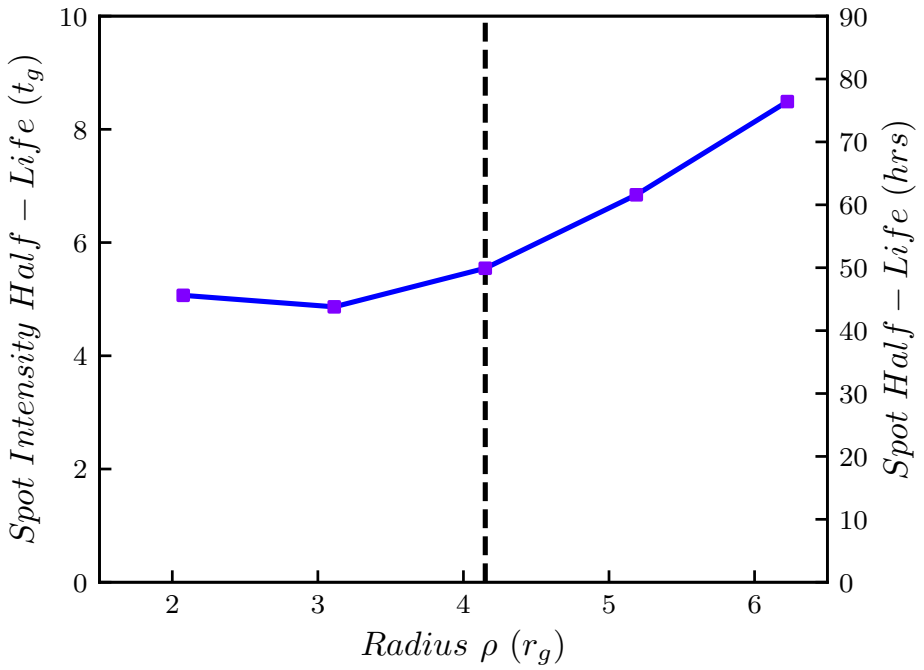

Figure 2.14: Spot intensity decay time as function of cylindrical radial launch position ρ for spots launched at $\phi = 270°$. The dashed vertical line corresponds to the cylindrical radius of the critical surface. Spot intensity decay time is relatively flat inside the critical surface but increases outside the critical surface.

EHT images. Material originating outside the velocity critical surface experience much less shear, producing no arcs in reconstructed images, and are thus distinguishable from interior spots in the image domain.

The evolution of structure in these spots is strongly dependent on the radial and azimuthal launch position of the material. While the azimuthal launch position of the spot dramatically alters the maximum intensity of the reconstructed image, the sheared structure remains qualitatively the same for fixed launch radii. Black hole driven spots exhibit high maximum intensities but fall to quiescent jet intensities within a couple of days, and exhibit multi-modal features in their light curve. Exterior spots exhibit lower maximum intensities for most azimuthal launch positions but persist for much longer, and can contribute to the light curve for over a week. Changing the azimuthal launch position of a spot can alter the maximum intensity by up to a factor of 5 due to differences in beaming around the jet. By combining the spot maximum intensity, half-life, and light curve structure, it is possible to distinguish black hole driven and wind driven spots, and possibly constrain the formation and launching character of AGN jets.

These distinctions persist in the visibility data, which may be used to probe jet launching physics without using image reconstruction. In a future publication we hope to explore how visibility data can also help distinguish between black hole driven and wind-driven relativistic jets.

The publication of the black hole image from the EHT observations taken in 2017 signify the start of a new era of horizon-scale science. While those results primarily focused on image features, direct GRMHD comparisons, and geometric modeling Event Horizon Telescope Collaboration et al. (2019d,e,f), incorporating semi-analytic models into the feature-extraction pipeline is a key goal for EHT analyses going forward. In particular, adding both the force-free jet and shearing spot model as described in this work to the THEMIS model comparison framework (Broderick et al., 2020) will allow for precise estimates of jet launching mechanisms and tight constraints on time variability. The shearing spot model is designed to be compatible in an arbitrary velocity field, and can also be used to model time variability in SMBH systems without jets, or with more exotic velocity profiles.

Chapter 3

Accretion Flow Dynamics and Black Hole Mass Estimates

The structure and physics of material within a hundred gravitational radii of supermassive black holes is an area of active research and discovery. Early models for how the gas around SMBH must behave describe geometrically thin, optically thick gas disks, where some kind of viscosity transports angular momentum out of the disk, causing the gas to sprial down onto the central black hole (Shakura & Sunyaev, 1973). These so-called $\alpha - disk$ models, after the coefficient representing viscosity, work rather well at describing the temperature structure and spectrum of small solar-mass sized black holes, and highly active, high-accretion rate SMBHs.

However, there exists a large population of AGN with low accretion rates and a very broad-band spectrum, which cannot be adequately characterized by classic $\alpha - disk$ prescriptions. A different model is preferred, where instead of a geometrically thin, optically thick disk, the surrounding gas is geometrically thick and optically thin. These systems have much lower gas densities, and as such cool inefficiently. This produces very high temperatures compared to α *disk* models, and instead of radiating out through the disk, most of the energy in the gas is physically advected onto the black hole, leading to their categorization as Advection-Dominated Accretion Flows, or ADAF (Narayan & Yi, 1995; Narayan et al., 1998).

The generalization of ADAF systems is the RIAF, or Radiatively Inefficient Accretion Flow. As the name implies, these systems lose relatively small amounts of energy through radiation, and instead much of the energy content of the gas is advected on to the black hole. RIAF models have been very successful at characterizing the shape of broad, low-

luminosity AGN spectra like Sgr A* and M87.

Beyond a few dozen gravitational radii, it is not clear if the RIAF/ADAF description of the accretion flow remains valid. While the radial density, temperature, and pressure profiles all settle into power-laws beyond 100 r_g, the gas at 10^{4-5} r_g may look very different.

3.1 Estimating Black Hole Masses

Accurately estimating the SMBH masses is difficult due to the small spheres of influence, the region where the SMBH dominates the gravitational potential, and complicated nature of galactic centers. A number of methods have been employed, with varying breadth of application and measurement precision. These include applications of the Eddington limit (Mazzucchelli et al., 2017), to the inversion of the Galaxy-BH scaling relations (Ferrarese, 2002), and line reverberation mapping (Blandford & McKee, 1982; Peterson & Bentz, 2011; Shen, 2013), all of which provide rough estimates of SMBH masses subject to various assumptions regarding AGN, their environments, and their relationships to their hosts. More precise measurements, which provide the foundation for the empirical methods mentioned above, are obtained by modeling the motion of stars or gas in the nuclear region of the host galaxy (see, e.g., the review by Kormendy & Ho, 2013). In both cases, the underlying assumption is that relevant emitters are probes of the local gravitational potential, and thus when well within the sphere of influence of the central SMBH, its mass. Characterizing gas motion around the central SMBH is critical to understanding how these objects accrete, and in turn how these accreting engines feedback on their host galaxies.

For the stellar-dynamical mass measurements, it is the velocity distribution of the stars that is employed as the probe of the gravitational potential. In this case, the stars are presumed to be on ballistic orbits, determined by a gravitational potential set by both the central SMBH and the nuclear star cluster. Typically, individual stars are not resolved, admitting only measurements of integrated line shapes. Thus, based on the distribution of light, average spectra, and line shapes, the distribution of stellar masses, orbits, and mass distribution is reconstructed (Kormendy & Richstone, 1995; Gebhardt & Richstone, 2000; Gebhardt et al., 2011). In contrast, for the gas-dynamical mass measurements, it is the velocity distribution of the orbiting ionized or molecular gas that is employed. Typically, it is assumed that the gas is confined to a thin disk on circular Keplerian orbits, where the enclosed mass is estimated by directly applying Kepler's Law. In many cases, while the line-of-sight velocity profile may be well described by a thin Keplerian disk, the velocity dispersions are not; the observed velocity dispersions can be up to an order of magnitude larger than predicted by the Keplerian disk model. There have been attempts to account

for the extra dispersion via additional pressure corrections, but it is not clear that this is well justified – in many cases the effective temperatures associated with the observed velocity dispersions is well in excess of that necessary to destroy the molecules responsible for the observed line emission (Macchetto et al., 1997; Barth et al., 2001; Neumayer et al., 2007; Walsh et al., 2010).

For a handful of objects, SMBH mass estimates have been obtained using both methods, affording an opportunity to directly compare them. While these are generally consistent in a number of nearby cases (Davies et al., 2006; Pastorini et al., 2007; Neumayer et al., 2007; Cappellari et al., 2009), in nearly half there is a systematic difference between the stellar-dynamical and gas-dynamical mass estimates (Verdoes Kleijn et al., 2002; de Francesco et al., 2006; Gebhardt et al., 2011; Walsh et al., 2012, 2013), with the latter typically being significantly smaller. In a recent case, M87, this difference is roughly a factor of two, with the stellar-dynamical modeling finding a mass of $6.6 \pm 0.4 \times 10^9 M_\odot$ while the gas-dynamical modeling finds $3.5^{+0.9}_{-0.7} \times 10^9 M_\odot$. This has clear implications for the (in)efficiency of M87's jet and current millimeter wavelength Very Long Baseline Interferometry (mm-VLBI) observations which promise to resolve the putative horizon.

Sagittarius A* (Sgr A*), the SMBH at the center of the Milky Way, provides an elucidating example. It has the virtue of having the most accurately measured mass of any SMBH, $4.3 \pm 0.3 \times 10^6 M_\odot$, obtained via the observation of orbiting massive stars (Gillessen et al., 2009b,a; Ghez et al., 2009).[1] It also has a variety of historical gas-dynamical mass measurements, the earliest of which had similar spatial resolution, measured in terms of the size of the sphere of influence of the central SMBH, as those recently reported of extragalactic SMBHs (Lacy et al., 1979, 1980). That is, by measuring the velocities and disperisions of lines emitted by ionized gas clouds, Lacy et al. (1980) estimated a central SMBH mass of $2.4 \times 10^6 M_\odot$, albeit with 100% error.[2]

For Sgr A*, the reason for the discrepancy is clear. Subsequent observations of the Galactic center have fully resolved the ionized gas within the sphere of influence of the SMBH. Contrary to the assumption in Lacy et al. (1980), the gas does not move along circular, Keplerian orbits. Rather, it is organized into the "mini"-spiral, a pc-scale structure with multiple arms and distinct non-Keplerian motions (Becklin et al., 1982; Montero-Castaño et al., 2009; Irons et al., 2012). The origin of the structures in the Galactic

[1] This differs from stellar-dynamical mass measurement in that Sgr A* provides the only example for which individual stars may be resolved and tracked on decadal timescales. The orbital of S2, one of the massive stars used for this purpose, passes within 120 au of the SMBH and has a period of 16 yr.

[2] While Lacy et al. (1980) reports a mass of $3 \times 10^6 M_\odot$, they assume that the Galactic center is at a distance of 10 kpc; we provide the value after correcting this distance to 8 kpc, consistent with the most recent measurements.

center is the larger-scale, tri-axial Galactic potential, and its interaction with the molecular torus at 3 pc (Eckart et al., 2002; Schödel et al., 2002; Genzel et al., 2010). When the non-Keplerian, non-circular gas structures are modeled, the revised gas-dynamical mass estimate is $4.5 \times 10^6 M_\odot$, in agreement with that derived from stellar orbits (Irons et al., 2012).

Even outside our own galaxy, when the nuclear gas disk is well resolved and gas velocity profile carefully mapped, the mass estimate from gas kinematics is entirely consistent with stellar dynamics mass estimates (Davis et al., 2017; Boizelle et al., 2019). However, in galaxies where there is not a well-resolved disk, there are theoretical reasons to believe that, in sub-Eddington systems, inside the Bondi radius the gas does not lie on Keplerian or near-Keplerian orbits (Narayan & Yi, 1994; Neumayer et al., 2007; Chan & Krolik, 2017; Imanishi et al., 2018). Hence, here we explore the impact of sub-Keplerian velocity profiles on gas-dynamical mass estimates.

3.2 A Summary of the 2013 M87 Gas Dynamics Mass Estimate

In order to place our project into the proper context we will briefly summarize the data, procedure, and principle results of Walsh et al. (2013). The authors of that paper used 2011 observations of the central nuclear region of M87 from the Hubble Space Telescope (HST) Space Telescope Imaging Spectrograph (STIS) instrument. The slits have a spectral resolution of 0.554 Å pixel^{-1} and a spatial resolution of $0\farcs0507$ pixel^{-1}. The G750M gratings were used, which cover the Hα and [NII] emission lines. The STIS slit was placed at 5 parallel, adjacent locations around the nucleus, with a position angle of 51°. The slits were exposed between 1521 and 2911 s using a dithering technique to suppress the contributions from cosmic rays. After processing the slit data with standard IRAF tasks, a final 2D spectral image was produced for each slit. Individual 1D spectra out to 0.5" were then produced from the 2D spectra after a simple linear continuum subtraction.

Each 1D spectra was then fit with three Gaussians corresponding to the three important emission lines, Hα, and [NII]. The velocity, velocity dispersion, and flux measurements were all taken based off the Gaussian fits to the 1D spectra. The spectra near the slit centers for the 2, 3, and 4 slits exhibits a blended complex of all three emission lines, and it proved challenging to differentiate the three Gaussian fits and produce reliable velocity data. Thus, the velocity data produced for the 1D spectra in the immediate central region was not included when trying to constrain the gas dynamics model.

The velocity curves are roughly consistent with rotating gas, and exhibits a sharp 1200 $\mathrm{km\,s^{-1}}$ central velocity gradient. The velocity dispersions range from 150 $\mathrm{km\,s^{-1}}$ to about 450 $\mathrm{km\,s^{-1}}$, but larger dispersions are expected in the unresolved center. The observed velocity profiles were modeled assuming the gas was undergoing circular rotation in a geometrically thin disk inclined with respect to the observer, and the rotation velocity of the gas depends on the central black hole mass, the galaxy mass-to-light ratio, and the central stellar mass profile. The model generates velocity profiles on a grid that matches the STIS resolution, and the velocity dispersion is modeled with a thermal component and a constant. The model disk was illuminated by fitting two offset, slightly elliptical Gaussian emissivity components, which was able to match the observed flux profile. The model velocity dispersions could not reproduce the observed velocity dispersions with only thermal and instrument broadening, and a constant 170 $\mathrm{km\,s^{-1}}$ was added in quadrature to the thermal and instrument dispersion as an intrinsic dispersion.

After optimizing the model fits against the observed velocity profiles the estimated black hole mass was determined to be $\left(3.5^{+0.9}_{-0.7}\right) \times 10^9 M_\odot$, with a gas disk inclination of 45^{+5}_{-7} degrees, and a systematic (recession) velocity of 1335^{+3}_{-9} $\mathrm{km\,s^{-1}}$. This black hole mass is inconsistent with the stellar dynamics mass estimate from Gebhardt et al. (2011) by at least 2σ, and consistent with the lower values of inclination from Macchetto et al. (1997).

3.3 An Extended Gas Dynamics Model for Estimating Black Hole Masses

Many prior attempts to explore deviations from Keplerian motion have been made. These typically invoke a turbulent effective pressure, $P_{\rm eff} = \rho\sigma^2$, within the gas disk (Neumayer et al., 2007), where σ is the disk velocity dispersion. In these pressure models, the modified orbital velocity is parameterized through the choice of $P_{\rm eff}$. In no case is a significant radial velocity considered.

In contrast, we parameterize the velocity profile directly, motivated by radiatively inefficient accretion flow (RIAF) models (Narayan & Yi, 1994; Blandford & Begelman, 1999; Chan & Krolik, 2017). These occur when the mass accretion rate at the black hole falls below 1% of the Eddington rate, and incorporate potentially substantial mass loss via winds, and describe the accretion flow inside the Bondi radius (Park & Ostriker, 1999). In the absence of fully specifying the gas disk structure, we parameterize the orbital and radial velocities directly

$$v_r = -\alpha v_k \quad \text{and} \quad v_\phi = \Omega v_k \tag{3.1}$$

for constants α and Ω, and v_k is the Keplerian velocity. For advection dominated accretion flow (ADAF) models, $\alpha \lesssim 0.1$, and $\Omega \lesssim 0.4$ (Narayan & Yi, 1995; Narayan et al., 1998). For RIAFs these can be more modest (Quataert & Narayan, 1999). This two parameter model does not directly address the physical origin for the modified accretion flow; doing so would require modeling the global structure of the flow. However, in principle, measuring α and Ω would provide a means to reconstruct the radial density and temperature profile. Even modest deviations of Ω from unity impose large systematic uncertainties on the reconstructed SMBH mass. Within the SMBH sphere of influence, assuming a circular Keplerian flow, the mass estimate is given by $M = rv_\phi^2/G = \Omega^2 M_{\rm true}$. Thus, setting $\Omega = 0.71$, consistent with RIAF models, would reduce the mass by a factor of 2. Less obvious is that the introduction of a non-zero radial velocity has significant implications for the velocity dispersion.

We approach the discussion of the systematic impact on SMBH mass estimates via M87, due to the recent disagreement between gas- and stellar-dynamical measurements. In doing so we follow closely the analysis of Walsh et al. (2013), adopting elements of their observational procedure and emission model. However, it should be understood that our conclusions are applicable to gas-dynamical mass measurements generally. In Section 3.4, we describe the disk model in detail and how emission lines are computed. Implications for spatially resolved spectral observations are presented in Section 3.5. In Section 3.6 we discuss the implications of our model for the mass of M87, and the implications for the gas dynamics estimates generally. We assume a distance to M87 of 16.7 Mpc (Bird et al., 2010; Cantiello et al., 2018).

3.4 Modeling Accretion Disk Line Profiles

As mentioned above, we approximately reproduce the procedure for modeling emission lines described in Walsh et al. (2013). Since gas dynamics mass estimates are predicated on the observation of nuclear emission lines, our model simulates the observation of emission lines from gas flows that exhibit sub-Keplerian motion. We assume the ionized gas lives in clouds with temperatures at or below $10^4 K$, and the clouds themselves move in the potential of the central black hole on virialized orbits. Once we model the intrinsic line shape for gas inside the clouds, we generate a parameterized cloud velocity field with separate radial and azimuthal components. This intrinsic line is then boosted to produce the correct intensity for a far away observer. Lastly, we light up our gas disk with a pair of emissivity profiles derived from observations of M87's nuclear region (Walsh et al., 2013) to produce line intensities approximately consistent with observations. This broadened line is then

smeared in the image space with an elliptical Gaussian kernel simulating the resolution of the STIS instrument.

For a gas emission line, the general line shape is a Voigt profile, a combination of Gaussian and Lorentzian components (Padmanabhan, 2000). However, far from the galactic nucleus, the observed line widths are typically very narrow, implying that the processes responsible for the Lorentzian component (pressure broadening, natural line width) may be neglected (Neumayer et al., 2007; Walsh et al., 2013). Thus, we model the natural line with a Gaussian profile

$$\phi_0(\nu) = \frac{1}{\sqrt{2\pi\Delta\nu_D^2}} \exp\left[-\frac{(\nu-\nu_0)^2}{2\Delta\nu_D^2}\right], \quad \text{where} \quad \Delta\nu_D = \nu_0 \frac{\sigma}{c} \tag{3.2}$$

where σ is the velocity dispersion of the emitting gas, and ν and ν_0 are the thermally broadened rest-frame line frequency and unbroadened line center, respectively.

The existence of line emission near the galactic nucleus implies the temperature of the emitting gas must be less than $T \approx 10^4$ K, otherwise the emitting gas would be start to become fully ionized. However, measured central dispersions on the order of 100 kms^{-1} (Neumayer et al., 2007; Walsh et al., 2010, 2013) imply temperatures $> 10^6$ K if derived solely from thermal broadening, which should completely ionize the gas and preclude any line emission in the galactic nucleus. Therefore, the existence of wide emission lines near the galactic nucleus motivates a picture in which cooler, line-emitting clouds are embedded in a large-scale, partially virialized flow. In the limit of many such clouds, the resulting lines will be Gaussian with line widths dominated by the dispersion in the turbulent cloud velocities. This is similar to the description and structure of Broad Line Regions in quasars, and its application here at low redshifts in the local universe is relatively novel.

From the virial theorem, the line-of-sight dispersion velocity σ is related to the gravitational potential energy via

$$\sigma^2 = f\frac{GM}{R}. \tag{3.3}$$

where M is the mass enclosed at a radius R, and f is a numerical factor, typically of order unity for a purely virial, dispersion supported system. For a thin gaseous disk, it is possible to relate the height to the temperature via $h = r(c_s/v_k)$, where c_s is the speed of sound. For a monatomic ionized gas

$$(c_s)^2 = \frac{5}{3}\frac{P}{\rho} = \frac{5}{3}\frac{kT}{\mu m_p} \tag{3.4}$$

where P is the pressure in the disk, ρ is the density, T is the gas temperature, $\mu = 0.6$ is the mean molecular weight for an ionized disk, and m_p is the proton mass. It is possible to define a virial temperature as $kT_{vir} \approx GMm_p/r$, and then define the disk scale height as

$$\frac{h}{r} = \left(\frac{5}{3\mu}\right)^{\frac{1}{2}} \left(\frac{T}{T_{vir}}\right)^{\frac{1}{2}} \approx 1.67 \left(\frac{T}{T_{vir}}\right)^{\frac{1}{2}}. \tag{3.5}$$

When a disk is turbulent, it is possible to use T as an effective temperature to describe both thermal and turbulent contributions to the gas motion, and we can then replace c_s with the σ from above, giving

$$\sigma^2 = (v_k)^2 \left(\frac{h}{r}\right)^2 \sim \frac{GM}{r} \left(\frac{h}{r}\right)^2 \tag{3.6}$$

For very cold disks, h/r can be small, but for a typical RIAF, $h/r \sim 0.3$ so $\sigma^2 \sim 0.1GM/R$, or $f = 0.1$.

It is also possible to empirically estimate f using the observations in Walsh et al. (2013) assuming the gas dispersion can be entirely associated with an effective temperature, with both turbulent and thermal components. The minimum velocity dispersion is measured to be about 150 km s^{-1} at 40 pc from the center. For a fully virial, dispersion supported system with the same central mass, this velocity dispersion should occur at a radial distance of $\approx$ 400 pc. We thus adopt an $f = 0.1$ going forward, as the ratio of these distances is consistent with the predicted numerical factor for an RIAF type disk.

We model the the global gas cloud motion assuming the clouds lie in a thin disk around the central black hole, tilted at an inclination i with respect to the observer's line of sight. The velocity field, $\vec{\beta}$, of this disk is parameterized with a radial and azimuthal component

$$\vec{\beta} = \frac{v_r}{c}\hat{r} + \frac{v_\phi}{c}\hat{\phi}, \tag{3.7}$$

where v_r and v_ϕ are given in Equation (3.1), and $\hat{r}$ and $\hat{\phi}$ are the radial and azimuthal unit vectors relative to the central black hole and aligned in the normal way with the disk axis. We can rewrite this in terms of Cartesian coordinates X and Y, defined such that the Z-axis is aligned with the disk axis, and the X-axis is parallel to the observer's x-axis:

$$\begin{aligned}\vec{\beta} &= \frac{v_r}{c}\left(\frac{X}{R}\hat{X} + \frac{Y}{R}\hat{Y}\right) + \frac{v_\phi}{c}\left(-\frac{Y}{R}\hat{X} + \frac{X}{R}\hat{Y}\right) \\ &= \left(v_r X - v_\phi Y\right)\frac{\hat{X}}{Rc} + \left(v_r Y + v_\phi X\right)\frac{\hat{Y}}{Rc}.\end{aligned} \tag{3.8}$$

For a distant observer with a line of sight, $\vec{k} = \cos i\ \hat{Z} + \sin i\ \hat{Y}$, the projected velocity, $\vec{k} \cdot \vec{\beta}$, is

$$\vec{k} \cdot \vec{\beta} = \frac{\sin i}{Rc} \left(-\alpha v_k Y + \ \Omega v_k X\right), \tag{3.9}$$

where we have expressed v_r and v_ϕ in terms of v_k as described in Equation (3.1).

We construct the observed line shape, including Doppler beaming and the Doppler shift, via the Lorentz invariant I_ν/ν^3:

$$\phi(\nu) = g^{-3}\phi_0(g\nu) \tag{3.10}$$

where g is the standard Doppler factor,

$$g = \frac{1 - \vec{k} \cdot \vec{\beta}}{\sqrt{1 - \beta^2}}. \tag{3.11}$$

Finally, we use an empirically motivated emissivity model following the prescription outlined in Walsh et al. (2013), where the emissivity is modeled by fitting a number of Gaussian components to the observed light profile. In that work, the observed light profile is fit best by two offset elliptical Gaussians, but for clarity we use a pair of concentric circular Gaussians, j_1 and j_2:

$$\begin{aligned} j_1 &= A \exp\left(\frac{-R^2}{2r_1^2}\right) \\ j_2 &= B \exp\left(\frac{-R^2}{2r_2^2}\right), \end{aligned} \tag{3.12}$$

where r_1 and r_2 are the widths of the emissivity profiles, and A and B are numerical scaling factors. For M87, we adopt the values $r_1 = 6.6$ pc and $r_2 = 23.7$ pc, and $A = 26.5$, $B = 1.0$ in arbitrary flux units. These emissivity values are the same as those in Table 1 in Walsh et al. (2013). The observed line intensity is then

$$I_\nu = (j_1 + j_2)\, \phi(\nu), \tag{3.13}$$

and the model flux along the slit is then scaled to be of order 10^{-17} ergs^{-1}cm^{-2}.

We produce a $2.42'' \times 2.42'' \times 393$Å data cube representing x and y pixel coordinates and λ, respectively, in the image plane, with a $0.01''$ spatial resolution and a 1 Å wavelength resolution centered on 6548 Å, the natural line frequency of [N II]. To project the image

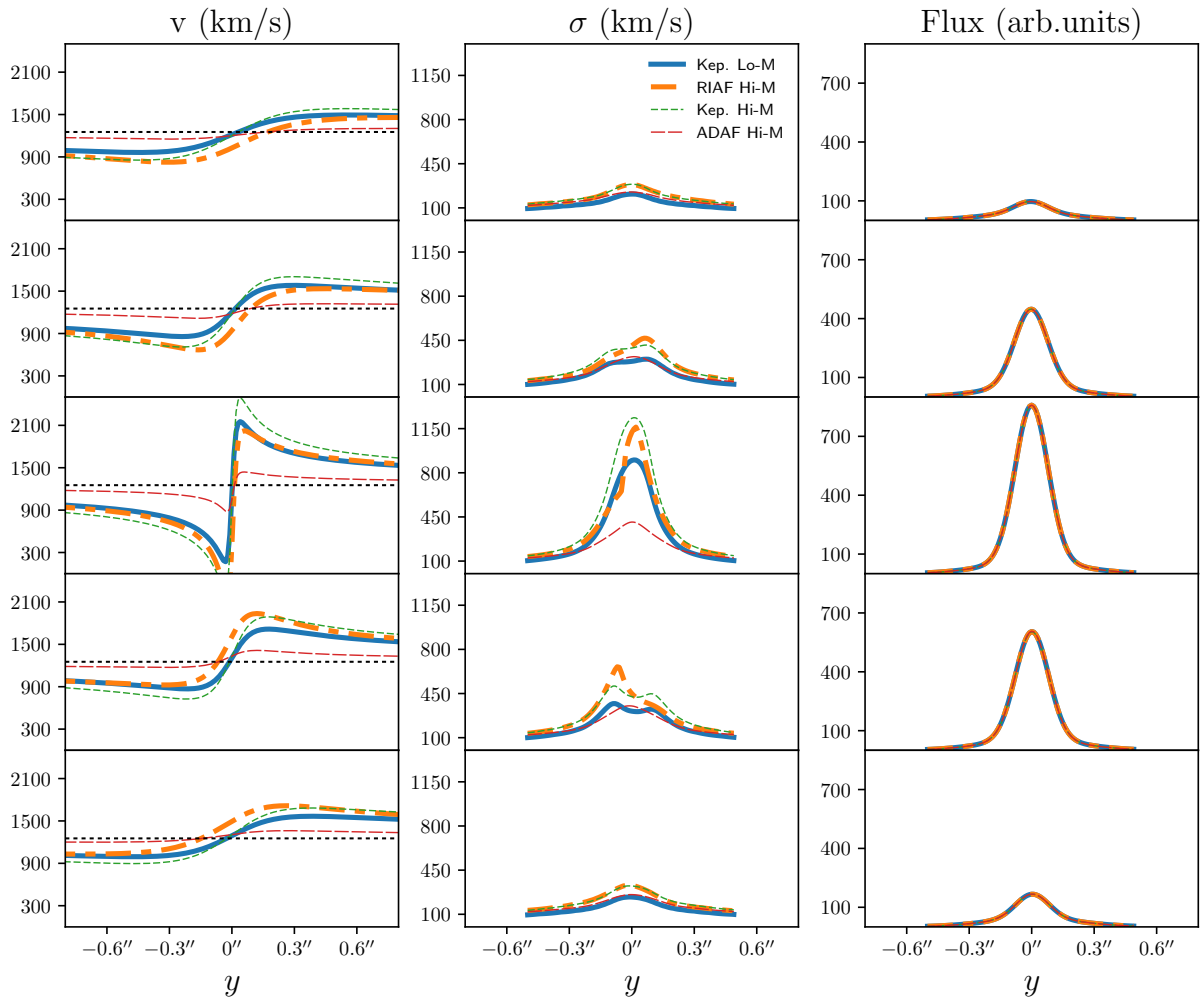

Figure 3.1: Line-of-sight velocity (left), dispersion (middle), and integrated flux (right) along the slit vertical axis for five different horizontal slit positions. From the top row, and centered on the black hole, the first slit is centered at $x = -0.2''$, the second slit at $x = -0.1''$, the third slit at $x = 0.0''$, the fourth slit at $x = 0.1''$, and the fifth slit at $x = 0.2''$. The Keplerian low-mass model is is plotted as a thick solid blue line in all columns, the RIAF high mass model as a thick orange dashed-dotted line, the Keplerian high-mass model as a thin green dashed line, and the ADAF model as a thin red long-dashed line.

plane onto the disk, we counter-rotate the data cube by a position angle ϑ and then tilt by an inclination i:

$$X = x\ \cos\vartheta - y\ \sin\vartheta, \tag{3.14}$$

$$Y = \frac{x\ \sin\vartheta + y\ \cos\vartheta}{\cos i} \tag{3.15}$$

where the $\vartheta = 6°$ and $i = 42°$ are again taken from measurements in Walsh et al. (2013). We simulate an HST spectrograph observation by convolving the data cube with a elliptical Gaussian kernel with standard deviations $\sigma_x = 0.1''$ and $\sigma_y = 0.0507''$, which has the effect of blurring the spectral features in the image plane.

3.5 Exploring Systematics in Black Hole Mass Estimates

3.5.1 Gas Disk Velocity

In order to characterize any differences in velocity and dispersion profiles between Keplerian and non-Keplerian velocity flows, we simulate observations at five different x-locations, corresponding to slits, covering the inner $0.5'' \times 1.0''$ region centered on the black hole. For each of these simulated observations, we extract the velocity and integrated flux along the y-direction, and construct the dispersion by using spline interpolation to find the FWHM of the blurred line profile.

The only parameters that we vary between each model are the central black hole mass M and the values for α and Ω. Our baseline model is an attempt to produce similar results to those in Walsh et al. (2013), and has a black hole mass of $3.5 \times 10^9 M_\odot$ and circular, Keplerian velocity field: $\alpha = 0$ and $\Omega = 1.0$. We also produce a model with circular Keplerian velocities for the mass estimate from Gebhardt et al. (2011), $M = 6.6 \times 10^9 M_\odot$, where $\alpha = 0$ and $\Omega = 1.0$.

We compare these to two non-Keplerian velocity profiles, assuming the high-mass estimate for the black hole mass in both. Following Narayan & Yi (1995), we consider an ADAF-like velocity profile, with $\alpha = 0.072$ and $\Omega = 0.2$, arising from their self-similar model (see Fig. 1 of Narayan & Yi, 1995). We also consider a more modest sub-Keplerian flow, similar to RIAF models, for which we set $\alpha = \sqrt{0.1}$ and $\Omega = \sqrt{0.7}$.

We compare radial velocity, velocity dispersion, and flux along the y-direction for these four models in Figure 3.1. The Keplerian low-mass model represents the typical model

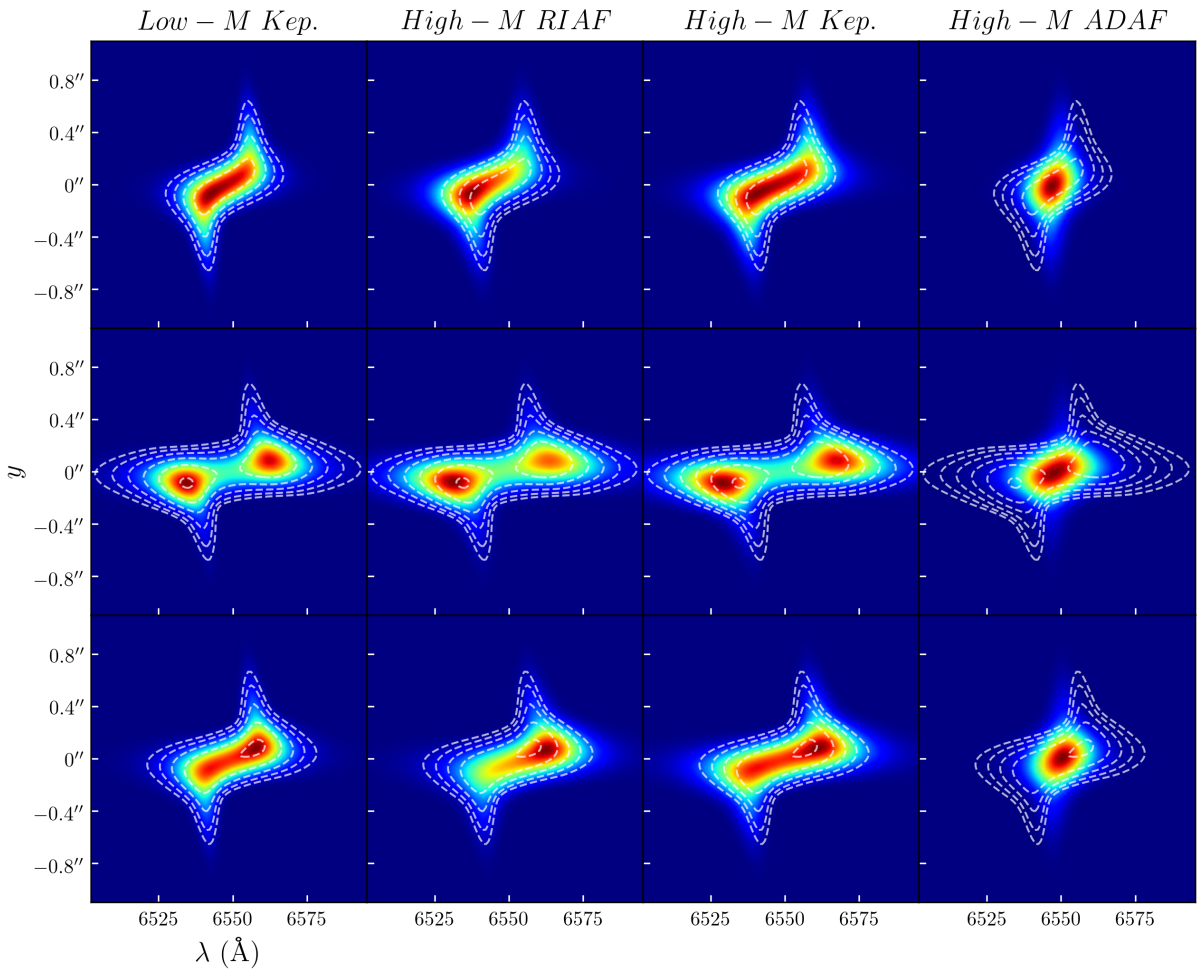

Figure 3.2: 2D spectra along the slit for a the case of a low-mass central black hole with a Keplerian velocity field (first column), a high-mass central black hole with a sub-Keplerian (RIAF) velocity field (second column), a high-mass black hole with a Keplerian velocity field (third column), and a high-mass central black hole with an ADAF velocity field (fourth column). The top and bottom rows correspond to slits centered 0.1″ away from the central slit. White dashed contours for the low-mass Keplerian model are shown in all panels.

for ionized gas motions in SMBH mass estimation experiments. In this model, the gas has no radial velocity component, and the azimuthal velocity component is equal to the circular Keplerian velocity. The velocity curves are approximately consistent with the

model produced by Walsh et al. (2013), and produce the expected symmetry across the slit center. The dispersions produced in our model are different than in typical gas-dynamical modeling, and generally produce higher intrinsic dispersions.

Unlike Walsh et al. (2013), we assume a spatially variable turbulent dispersion, increasing with the virial temperature as described in the previous section. This produces two notable effects in the dispersion plots: the first is a higher dispersion away from the slit center compared to the gas dynamical models presented, e.g., in Walsh et al. (2013). Second, there is a higher peak dispersion in the slit center. The first effect almost entirely mitigates an observational discrepancy between the modeled and observed dispersions in Walsh et al. (2013) and others, where an additional ~ 100 km s^{-1} is added to the modeled constant dispersion to achieve closer fits to observed data. The second effect only produces higher dispersions than other works in the center of the central slit, where the virial dispersion can reach as high as 900 km s^{-1}, much higher than the order 100 km s^{-1} seen in constant-dispersion models. Both of these effects are sensitive to the radial emission profile in the disk.

The high black hole mass Keplerian model produces qualitatively different velocity and dispersion profiles than the low-mass Keplerian model. The velocity curves are still symmetric around the center, but all slits exhibit higher peak velocities, up to 200 km s^{-1} higher than the low-mass Keplerian model in the central slit. The ADAF model produces radial velocities that are dramatically suppressed compared to the low-mass Keplerian model, even though the black hole mass used for the ADAF model is the same as the high-mass Keplerian model. The RIAF model is most similar to the low mass Keplerian model for the radial velocity curves, and in the central slit the velocity curves for the RIAF and low-mass Keplerian model effectively coincide. In the other slits, the RIAF velocity curve looks like the low-mass Keplerian curve, but shifted approximately $0.1''$ right or left depending on whether the slit is to the left or right of the central slit. The RIAF velocity profile is still similar to the low-mass Keplerian curve outside the inner $0.6''$ in all slits. Due to typical observational uncertainties, a gas disk exhibiting even substantially non-Keplerian motions could be mistaken for a Keplerian gas disk with a smaller central black hole mass, given only the velocity data.

The RIAF model is distinguishable from the low-mass Keplerian model in the distribution and magnitudes of the velocity dispersions. The RIAF model produces higher dispersions in the inner $0.6''$ than the low-mass Keplerian model, and even produces higher dispersions than the high-mass Keplerian model in outer slits. In the central slit, the RIAF model produces peak dispersions very near the high-mass Keplerian model, roughly 300 km s^{-1} higher than the low-mass Keplerian model. Another significant feature of the RIAF dispersion profile is the narrower peak in the central slit. Because of this, the RIAF

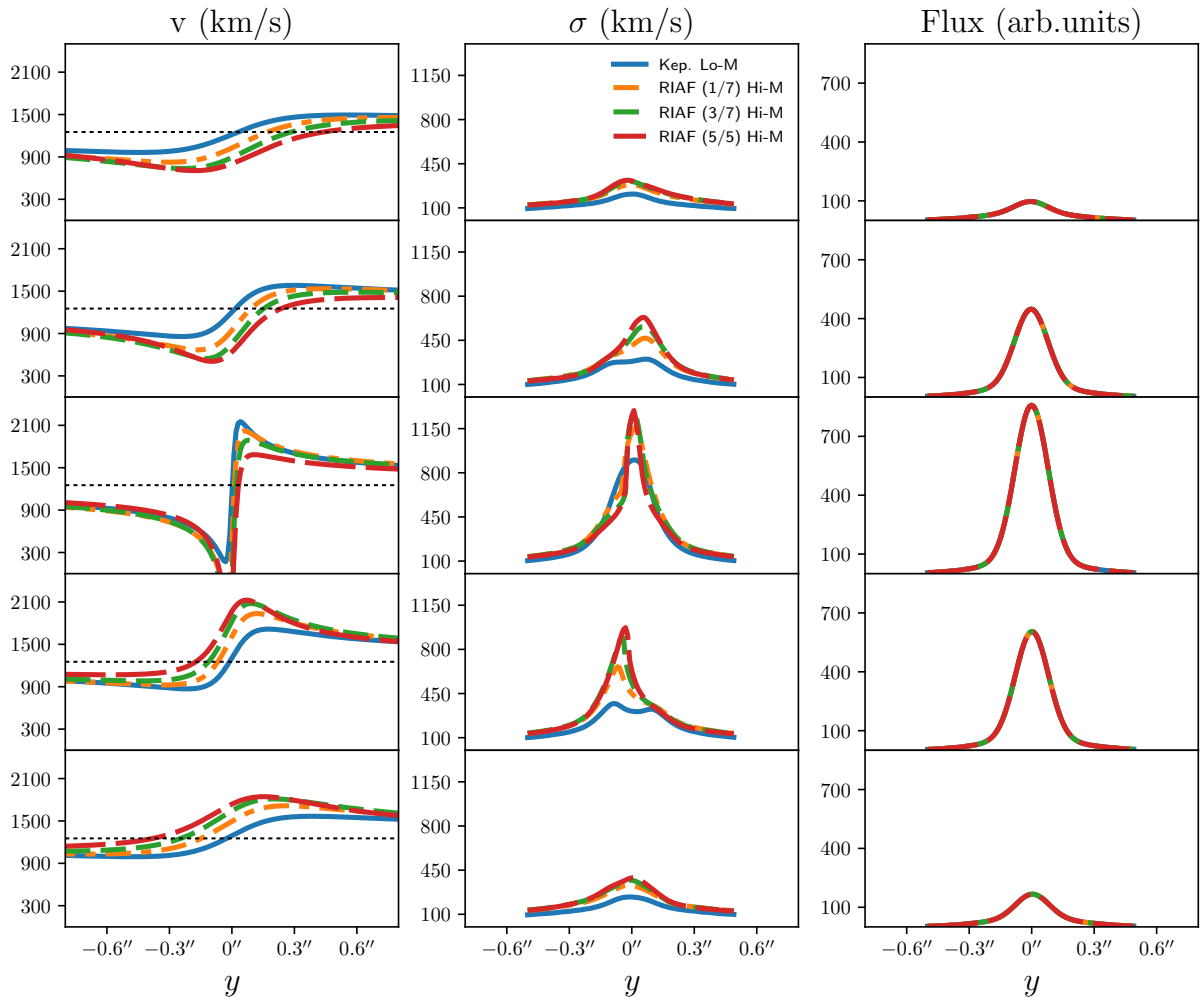

Figure 3.3: Line-of-sight velocity (left), dispersion (middle), and integrated flux (right) along the slit vertical axis for five different horizontal slit positions. The slit positions are the same as in Figure 3.1. The Keplerian low mass model is is plotted as a solid blue line in all columns, the slightly radial RIAF high-mass model as an orange dashed-dotted line, the RIAF model with additional radial motion as the green dashed line, and the RIAF model with even distribution of radial and azimuthal motion as the red long-dashed line

model produces qualitatively the same dispersions as the low-mass Keplerian model outside of the inner 0.2″. While the peak dispersion is higher than the low-mass model, in practice

distinguishing the RIAF and low-mass Keplerian model in the central slit may be difficult if the slit resolution is poor. However, outside the central slit, the RIAF dispersions are generally higher than those associated with the low-mass Keplerian model, and exhibit asymmetries due to the radial gas motions, and are, therefore, capable of distinguishing between the two models.

The high mass Keplerian model produces dispersions in the central slit almost 400 km s^{-1} higher than the low-mass Keplerian model, peaking near 1200 km s^{-1}. The ADAF model produces velocity dispersions that are very similar to the low-mass Keplerian model in every slit except for the center slit. In the center slit, the ADAF dispersion is lower than any other model by at least 300 km s^{-1}, and is qualitatively distinguishable from the low-mass Keplerian model. This further supports the conclusion that spatially resolved velocity dispersions provide a key signature of non-Keplerian flow velocities.

In Figure 3.2 we produce spatially resolved spectra for the three innermost slits by projecting the emission line profile along the slit y-direction. These spectra are "2D" in the sense that we are plotting the line intensity as a function of position along the slit and spectral wavelength. Dashed contours in this figure are emission intensities for the low-mass Keplerian model, and are plotted to facilitate comparisons with other models, and the rest-frame wavelength is 6548$\mathring{A}$.

In the central slit, the RIAF model produces a similar spectral profile to the low-mass Keplerian model, peaking approximately at the same frequency and producing the same intensity distribution across the slit. The primary difference between the RIAF and low-mass Keplerian spectra is the asymmetry in intensity between the long and short wavelength peaks. In the Keplerian model, both peaks have approximately the same intensity, but long wavelength peak in the RIAF model is dimmer than the short wavelength peak, compared to both models. When we compare the low-mass Keplerian and high-mass Keplerian models, we can see that the high-mass Keplerian model produces a wider emission profile in wavelength. The emission peaks in the high-mass Keplerian model are less coincident in wavelength with the low-mass model than even the RIAF model. The ADAF model is qualitatively different from the low-mass Keplerian model, and produces little to no emission outside 6525$\mathring{A}$ and 6575$\mathring{A}$.

In the outer slits, the RIAF model still has a similar emission profile to the low-mass Keplerian model, but red- or blue-shifted approximately 10$\mathring{A}$ depending on which side of the disk the slit observes, and the emission peaks preferentially in the same direction as the Doppler shift. The high-mass Keplerian model again produces more emission across wavelengths, and the central emission ridge (orange and red regions in Figure (3.2)) is larger than in the low-mass Kelplerian model. The ADAF model still produces a small

emission region compared to all the other models, and the emission peak is Doppler shifted from the rest wavelength by much less than the other models.

The line modeling done here is only for a single emission line. The observations in Walsh et al. (2013) measure the Hα and [NII] emission line complex, and the analysis produced in that work only incorporates data from spectra that had been satisfactorily decoupled. Close to the center, the line dispersions become large enough such that the three emission lines begin to overlap, and uniquely decomposing the lines becomes difficult. Since velocity and dispersion measurements in the very center are omitted in Walsh et al. (2013), it is difficult to compare this work with the observational results, as the most significant differences occur where line-decomposition becomes most difficult. The results of the modeling done in this work could exacerbate this issue; one of the key results of this work is increased dispersion for non-Keplerian models away from the center slit. This increase can blend nearby emission lines further out from the center, and make decomposition more difficult.

As mentioned above, it is possible to distinguish the low-mass Keplerian model from the RIAF model via a shift in the RIAF velocity curves when observing away from the central slit, and via increased and narrower RIAF dispersion profiles compared to the low-mass Keplerian model. To better characterize these differences, we produce radial velocity and dispersion curves for two more non-Keplerian models to explore the effects of increased radial velocities in Figure 3.3. These other two models both use the higher black hole mass, and have a total velocity magnitude equal to the high-mass Keplerian model. The first of these new models has a radial velocity component of $\alpha = \sqrt{0.3}$ and an azimuthal velocity component of $\Omega = \sqrt{0.7}$. Compared to our proto-typical RIAF model, this has an increased radial velocity component. The other new model has $\alpha = \Omega = \sqrt{0.5}$. This model has an even larger radial velocity component, in exchange for a reduced azimuthal contribution.

As we increase the radial velocity, the velocity curves shift further left or right in the y-direction depending on the side of the disk we measure the dispersed spectra on, and become more peaked on that side of the shift. This shift can be as large as $0.3''$ for observations at the edges of the disk, but this shift is suppressed near the galaxy's center. In the center, increasing the radial velocity component produces a shift down in velocities, where the difference in peak velocities between the low-mass Keplerian and RIAF half-and-half model is approximately 400 km s^{-1}.

Increasing the radial velocities also produces narrower velocity dispersions in the center compared to Keplerian models, and models with the same total velocity magnitude have the same maximum dispersion in the center. Away from the galaxy center, models with increased radial velocities have systematically higher velocity dispersions across the disk

relative to Keplerian models, and produce peak dispersions shifted away from the center. Some asymmetry is expected when the disk axis is rotated (rolled) with respect to the observation axis, but as radial velocity components produce more dispersion away from the galaxy center, this asymmetry is magnified. A rotated disk can also produce a shifted velocity curve, even in the Keplerian case. However, radial velocity components contribute most to the line-of-sight velocity orthogonally to the azimuthal components. That is, radial velocities still contribute to the line-of-sight velocity at the slit origin, which shifts the velocity curve away from the Keplerian model, even when the disk is not rotated.

Observationally, Walsh et al. (2013) find the best-fit emissivity for M87 is two Gaussians with slight offsets from the center. This implies that there is no drop in emissivity within ≈ 5 pc of the galaxy center, which is the resolution of their slit. Close to the black hole, accretion disk temperatures should increase enough to photoionize the gas, reducing the emissivity near the center. As mentioned above, the virial temperatures easily reach 10^8 K at a distance of 10 pc from the galaxy center, which is just within the resolution of the observations. The null result of reduced emissivity near the galaxy center suggests either sub-virialized flows, or that the gas clouds act as shielding for the cooler line-emitting gas inside and remain undisrupted even close to the center.

3.5.2 Gas Disk Structure

All of the existing ionized gas dynamics mass estimates presume a thin, Keplerian disk. Here we relax the condition that the disk is thin, motivated by results from simulations which show significant disk thicknesses out to large radii (Narayan & Yi, 1994; Quataert & Narayan, 1999; Blandford & Begelman, 1999; Chan & Krolik, 2017).

To model a thick disk, we follow the same procedure outlined in above to model ionized line emission with the addition of a vertical density profile. However, instead of evaluating the line intensity at the disk equator, we evaluate along the line of sight to produce an integrated line intensity in the image plane. Since the disk has a height, the line of sight velocity has an additional contribution in the vertical direction,

$$\vec{k} \cdot \vec{\beta} = -\frac{\cos i}{Rc} \alpha v_k Z + \frac{\sin i}{Rc} \left(-\alpha v_k Y + \Omega v_k X\right), \tag{3.16}$$

where i is the inclination of the disk, X, Y and Z are the cartesian coordinates of the disk, oriented such that X is parallel to a distant observer's x axis, and Z is aligned with the disk axis.

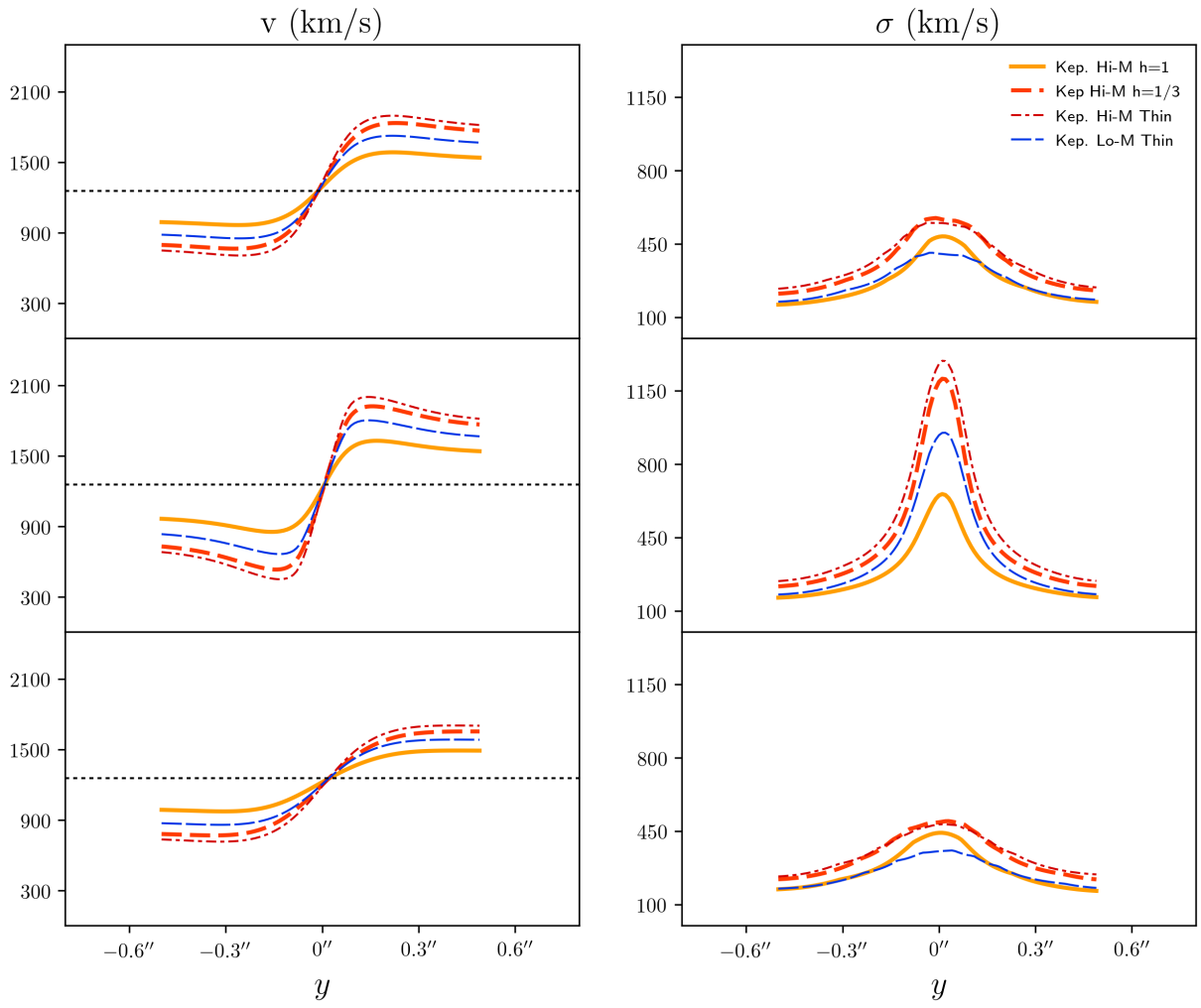

Figure 3.4: Simulated velocity and dispersion profiles for three slits placed across the central 0.3" of M87. All curves correspond to an optically thin Keplerian gas disk, but with different thick disk scale heights. The solid orange curve corresponds to a gas disk with scale height $h = R$, the dashed red curve to a gas disk with scale height $h = 1/3R$, the dashed-dot maroon curve to thin ($h << R$) gas disk, and the long-dashed blue curve to a thin gas disk with half the central black hole mass.

We assume the disk has a vertical Gaussian emission profile ρ, with a scale height $H = hR$ where h is a fractional parameter that determines the disk thickness as a function of the radial distance R from the center of the disk:

$$\rho = \frac{1}{\sqrt{2\pi H^2}} \exp\left(-\frac{Z^2}{2H^2}\right). \tag{3.17}$$

The ionized gas line shape is given by

$$\Phi = \int g^3(z,\nu)\phi_0(z,\nu)\rho(z)dz \tag{3.18}$$

where, for a given height element dz, g is the normal Doppler factor associated with the gas motion, ϕ_0 is the natural line profile (which we assume to be Gaussian), and ρ is the local density. We adaptively integrate Equation 3.18 along the line of sight to produce an integrated line shape. We then multiply this line profile by the spatial emissivity profiles measured in Walsh et al. (2013) to construct a line intensity map in the image plane.

Similar to the procedure from above, we conduct simulated observations of the intensity map to produce velocity and dispersion profiles at different x-positions in the image plane, analogous to Hubble STIS slits. The estimated line-of-sight velocity and dispersion curves are plotted in Figure 3.4 for the three inner-most slits, corresponding to slits with image plane x-positions of 0.1", 0", and -0.1", and span 0.5" to -0.5" in the image plane y-direction.

For modest disk thicknesses of $h = 1/3$ (thick, red, dashed line), similar to those seen in RIAF simulations at large radii, the line-of-sight velocity is suppressed by approximately $10 - 15\%$ at all y-positions relative to a thin disk with the same black hole mass (thin, maroon, dashed-dot line). For larger thicknesses, like $h = 1$ (thick, orange, solid line), the disk is quasi-spherical and the line-of-sight velocity is suppressed by nearly 50% relative to the geometrically thin disk of the same black hole mass. Large disk scale heights can even suppress the line-of-sight velocities well below that of a thin disk with a central black hole with half the mass. Here, the larger mass corresponds to the Event Horizon Telescope Collaboration et al. (2019f) black hole mass estimate of $6.5 \times 10^9 M_\odot$, and the lower black hole mass corresponds to the Walsh et al. (2013) mass estimate of $3.5 \times 10^9 M_\odot$.

Because we assume the disk is optically thin and inclined towards the observer at 42°, the overall effect of increasing the disk height is to suppress the line-of-sight velocities. In the forward half of the disk, closest to the observer, the line profiles from gas above the equatorial plane contributes more to the total line-of-sight velocity, which biases the gas velocities as if they were observed at a larger radius. Similarly for the back half of the

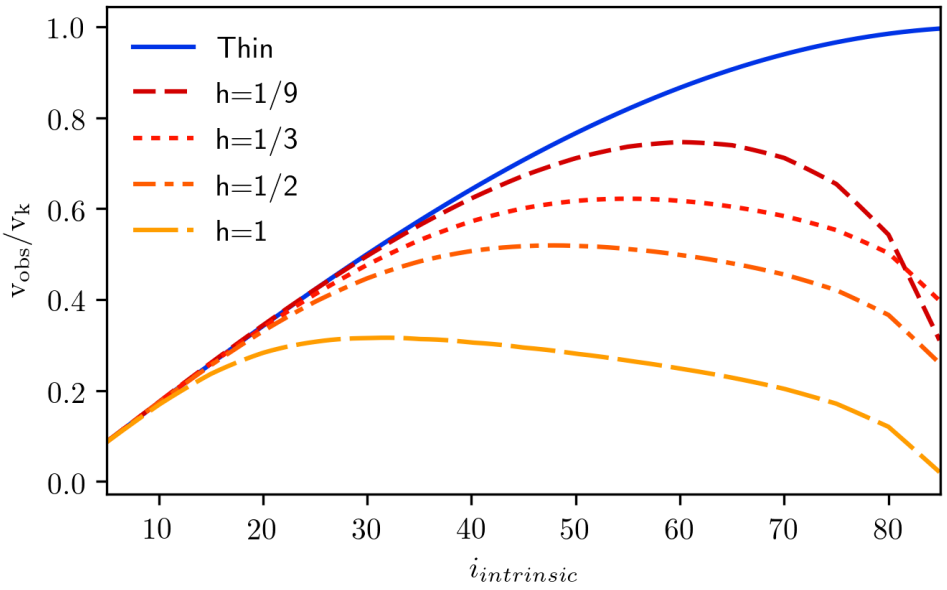

Figure 3.5: Ratio of observed velocity to orbital Keplerian velocity as a function of disk inclination for ionized gas disks of different thicknesses, with no intrinsic radial velocity.

disk, away from the observer, gas below the equatorial plane contributes more to the total line-of-sight velocity, producing the same velocity bias towards larger radii.

The observed line-of-sight velocity, v_{obs}, should be related to the intrinsic Keplerian orbital velocity v_k by

$$v_{obs} = \sin(i)F(i,h)\Omega v_k, \tag{3.19}$$

where i is the inclination of the disk, Ω is the fractional intrinsic sub-Keplerian factor of the gas, and F is the bias factor associated with the disk thickness. This F parameter should be dependent on both the disk inclination and the disk thickness.

In order to understand this bias factor F in the observed velocity, we produced simulated observations of Keplerian ($\Omega = 1$) gas disks with scale heights of $h = 1/9,\ 1/3,\ 1/2,$ and 1 with inclinations between 5° and 85°, incremented every 5°. We calculate the of the observed velocity to the orbital Keplerian velocity, and plot the result in Figure 3.5. Thinner disks (h=1/9, h=1/3) provide less suppression of the observed velocity than thicker disks, but still produce reductions in the observed velocity on the order of $30 - 40\%$. Very thick disks (h=1) provide significant suppression, upwards of 70%. As the disk becomes more

face-on (inclination approaches zero), the suppression factor from the intrinsic inclination dominates the observed velocity.

3.6 Applying the Existing EHT Mass Estimate

The measurement of a large black hole mass in M87 has a number of implications for the relationship between the black hole and its immediate environment. Large departures from non-axisymmetric motions would be difficult to reconcile with the nearly symmetric velocity profiles observed and theoretical expectations regarding the dynamics of gas flows, which are expected to efficiently symmetrize via viscous or magnetic interactions. The observed line-of-sight velocities of atomic line emission produced within the gas flow at 10–100 pc places now strong constraints on the dynamical state of gas on these scales and its relationship with the horizon and milliarcsecond-scale features. The gas velocity's low apparent value may indicate significantly different inclinations than those inferred from dynamical modeling or substantial departures from circular Keplerian motions (see, e.g., Kormendy & Ho, 2013; Jeter et al., 2019). Both of these are reasonable modifications to the pc-scale gas flow models.

In Figure 3.6 we show the implied constraint on gas orbital velocity and inclination arising from a simple, axisymmetric gas disk model that permits sub-Keplerian velocities. Note that because the Keplerian velocity at an angular displacement of θ is $\sqrt{GM/D\theta}$, this relationship depends on M/D directly when the gas flow velocity is scaled by the local Keplerian value. The width of the band primarily arises from the uncertainty in the measurement of M/D reported in Event Horizon Telescope Collaboration et al. (2019f), with a small contribution from the uncertainty in the gas velocity measurements from Walsh et al. (2013) added in quadrature.

There is no reason *a priori* to believe that the large-scale gas flows must be aligned with features on horizon scales. There is evidence that the radio jet has been reasonably stable over many Myr (see, e.g., Broderick et al., 2015). Nevertheless, at its present low accretion rate, even a highly misaligned accretion flow would require many orders of magnitude more time to substantially reorient the black hole spin.

Such a misalignment may be borne out in practice: even with the considerably larger black hole mass, it remains difficult to align the pc-scale gas flow with the inferred milliarcsecond-scale, and now horizon-scale, jet feature. Inclinations less than 27 degrees require super-Keplerian flows. This suggests that the gas-flow orientation is discrepant with the mas radio-jet by at least ~ 2 degrees. It is notable that the PA of the gas flow of 45 degrees

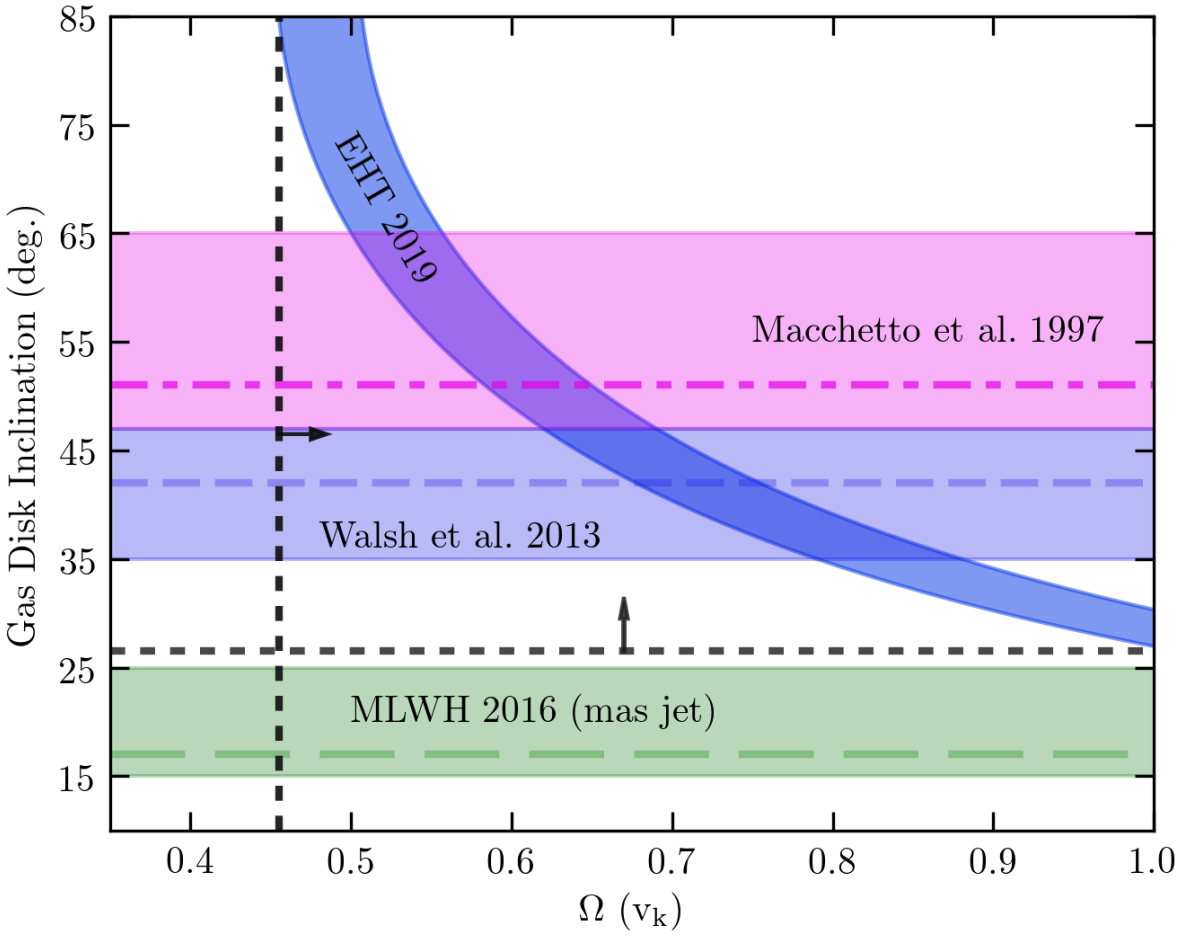

Figure 3.6: Constraint imposed by M/D measurement and observed gas velocities on the dynamics of the parsec-scale accretion flow in M87. The orange band indicates the range permitted by the measurements presented here when combined with the gas velocities in Walsh et al. (2013). The green horizontal band shows the range of mas-scale radio-jet inclinations; the blue and magenta bands show the measured inclinations from the gas-dyanmics measurements presented in Walsh et al. (2013) and Macchetto et al. (1997), respectively. Limits imposed by requiring $v < v_K$ and $i < 90$ degrees are indicated.

reported in Walsh et al. (2013) is consistent with the PA of the black hole spin implied by the PA_{FJ} estimates in Event Horizon Telescope Collaboration et al. (2019e,f). However, there is little direct evidence for these inclinations from direct observations of the gas disk itself.

Estimates of the gas disk inclination based on the geometry of the arcsecond-scale optical emission range from 47 to 64 degrees (Macchetto et al., 1997) and 35 to 47 degrees (Walsh et al., 2013). These require significantly sub-Keplerian gas flow velocities, ranging from 90% down to 44% of the Keplerian value. This limit is consistent with expectations from accretion models for low-luminosity active galactic nuclei, including non-radiative GRMHD simulations of gas flows onto black holes (see, e.g., Event Horizon Telescope Collaboration et al., 2019e, and references therein). In these models, substantial pressure gradients within the flow provide additional radial support, and thus the orbital velocity and vertical disk structure are related via $v/v_K \propto 1 - h^2/r^2$, where $h/r \sim 0.3$ is the ratio of the accretion flow height and radial position.

We can then take these observed velocity vs. inclination profiles from Figure 3.5 and plot thick disks as different bands in the inclination/sub-Keplerian space, as shown in Figure 3.7. Here we remove the inclination band from Macchetto et al. (1997) for clarity, and show the effective inclination for a disk with $h = 1/9$ as the dark-red shaded region, $h = 1/3$ as the red shaded region, and $h = 1/2$ as the orange shaded region. Since thick gas disks suppress the observed velocity in a similar way to inclination, a thick gas disk can have a larger inclination (more edge-on) than a thin gas disk and still have maintain relatively Keplerian gas velocities. Very thick gas disks (h=1) require super-Keplerian velocities for the observed line-of-sight velocities from Walsh et al. (2013) to be consistent with the EHT mass estimate.

Note that thick disks imply the gas disk inclination is generally more misaligned with the radio jet than thin disks. This is expected, since the bias in observed velocity we saw due to the thick disks permit the disk inclination to be greater than the inclination one would assume from a thin disk with the same observed velocity. If the gas disk is truly misaligned with the jet, it implies that the angular momentum of the large scale gas is different from the angular momentum of the black hole. This is not unexpected; the Bardeen-Peterson effect should align accretion disks with the black hole angular momentum, but is only effective at much smaller radii, very close to the black hole, and highly dependent on the surface density and viscosity prescriptions for the accretion disk (Bardeen & Petterson, 1975; Natarajan & Pringle, 1998). The Lense-Thirring precession timescales for low-luminosity systems like M87 can be as high as a Gyr, and again depend on the density and viscosity structure of the disk (Natarajan & Armitage, 1999). Thick accretion disks generally exhibit enough dynamical support to prevent alignment away from the inner most stable circular orbit

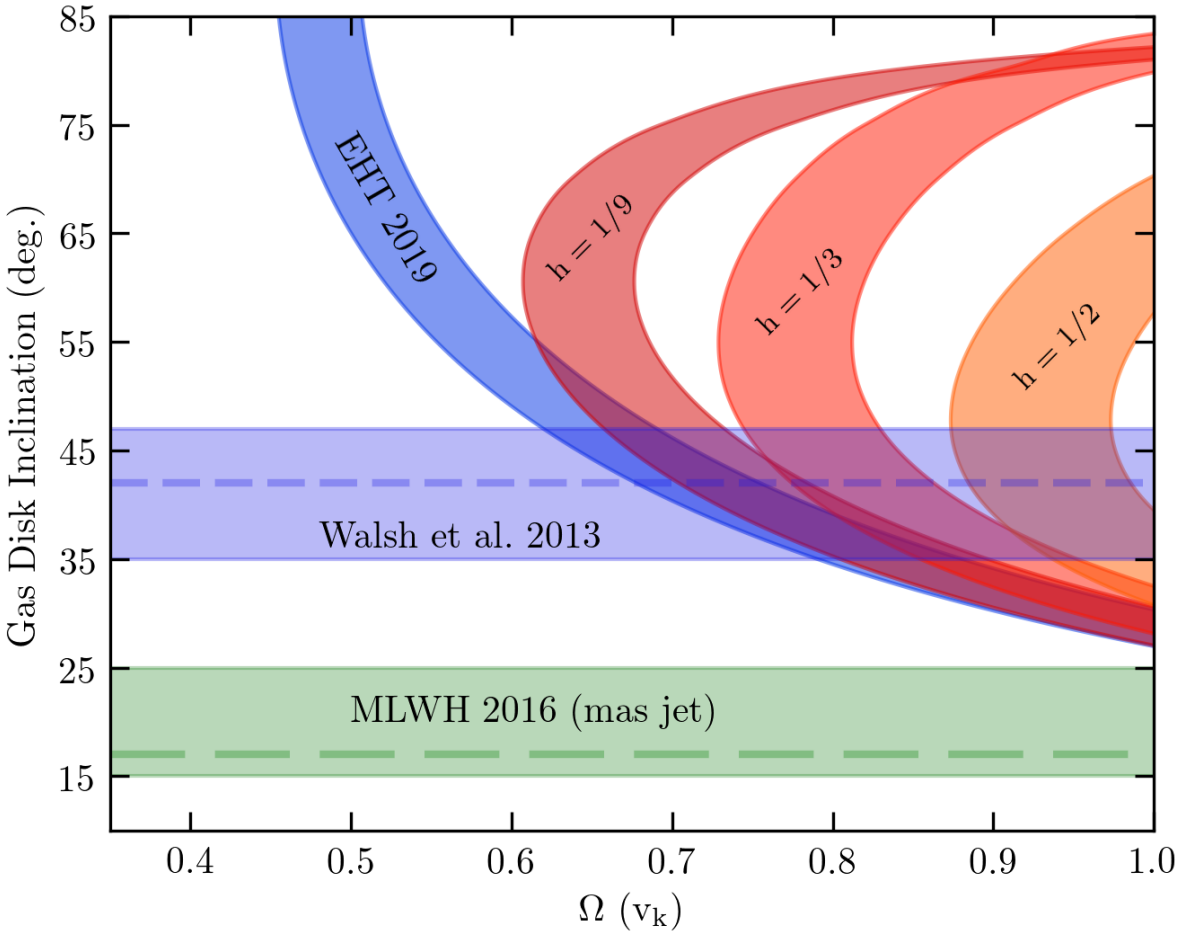

Figure 3.7: Similar to Fig. 3.6, now with brown (h=1/9), red (h=1/3) and orange (h=1/2) bands showing the effects of non-trivial disk height on the implied inclination and sub-Keplerian factor of the ionized gas disk. A disk with h=1 requires super-Keplerian intrinsic velocities to be consistent with the EHT mass estimate.

(ISCO) region, and end up producing solid-body-like rotations around the central black hole (Fragile & Anninos, 2005; Dexter & Fragile, 2011).

Thus it is not generally expected that the angular momentum of the large scale gas flow should be aligned with the black hole angular momentum. Such misalignments could arise from an asymmetrical mass distribution of the large-scale gas, or from an asymmetric galactic potential. Such an effect should be small in M87, since it has a relatively spherically symmetric radial stellar profile in the inner few dozen parsecs (Gebhardt et al., 2011), as well as a low velocity anisotropy (Zhu et al., 2014) at larger, Kpc distances.

3.7 Applications beyond the EHT

3.7.1 Implications for the Accretion Rate

M87 is notably a low luminosty AGN, with a jet power estimated between 10^{42} and 10^{44} erg/s^{-1} (Bicknell & Begelman, 1996; Stawarz et al., 2006; Bromberg & Levinson, 2009; Prieto et al., 2016). One may be concerned that the radial velocities described in this work may lead to an overestimation of the accretion rate, or a rapid depletion of the gas reservoir. Measurements of molecular line emission place conservative estimates on the gas mass in the inner 100 pc of M87 at about 3×10^6 $M_\odot$ (Tan et al., 2008). However, even if this gas reservoir is being depleted via a radial velocity component, much of that infalling matter will be redirected back out via winds and other outflows before it gets to the black hole.

For RIAF accretion solutions density scales as $r^{-3/2}$ or slower, meaning $\dot{M}$ scales as r^0 to $r^{0.5}$. This implies that as little as 0.3% of the gas in the disk gets down to the black hole (Blandford & Begelman, 1999). The mass accretion rate onto the black hole for this disk is can be expressed as the fractional accretion rate at the edge of the disk, or

$$\dot{M}|_{R_{\rm in}} = \epsilon \dot{M}|_{R_{\rm out}} = \epsilon v_r \Omega_D R_{\rm out}^2 \rho \tag{3.20}$$

where ϵ is the fraction of gas that reaches the black hole, v_r is the radial infall velocity, $R_{\rm in}$ is the radius where material must fall into the black hole, $R_{\rm out}$ is the edge of the accreting disk, Ω_D is the solid angle encompassing the disk, and ρ is the density of the disk. Integrating from the disk edge to the inner accretion radius allows us to express equation 3.20 as

$$\dot{M}|_{R_{in}} = \frac{\epsilon v_r}{2} \frac{M_T}{R_{out}} \tag{3.21}$$

where M_T is the total mass of the disk. For a radial velocity of $0.1v_k$, this implies a mass accretion rate of

$$\dot{M} = \frac{\epsilon\ (0.1\ v_k)}{2} \left(\frac{3 \times 10^6\ M_\odot}{100\ \mathrm{pc}} \right) = 2.43 \times 10^{-3}\ M_\odot \mathrm{yr}^{-1} \tag{3.22}$$

where v_k is the Keplerian velocity at 100 pc. This can be converted to a luminosity via

$$L = \eta \dot{M} c^2 = 1.36 \times 10^{43}\ \mathrm{ergs}^{-1} \tag{3.23}$$

where $\eta = 0.1$ is a typical efficiency factor for converting accreting matter into a jet luminosity.

For a radial velocity of $\sqrt{0.1}v_k \approx 0.3v_k$, the estimated accretion luminosity is 4.1×10^{43} ergs^{-1}. Thus for RIAF models with modest radial velocities, the estimated accretion luminosity is consistent with the observed jet luminosity. Even large radial velocities at significant fractions of the Keplerian velocity permit acceptable accretion luminosities. For a mass accretion rate of $\approx 10^{-3}\ M_\odot$/yr, a gas disk of $10^6\ M_\odot$ will deplete in $\approx$ 1Gyr, assuming no external replenishment.

3.7.2 Implications for the M-σ Relation

The correlation between the SMBH mass and bulge stellar velocity dispersions is one of the fundamental observational relationships between central black holes and their host galaxies. For large galaxies with high ($>$ 200 kms^{-1}) dispersions, and where SMBH masses have been estimated using both stellar dynamics and ionized gas dynamics, the stellar dynamics estimates produce higher black hole masses, as mentioned in Section 1. Motivated by this discrepancy, and by the difficulty in modeling high line dispersions in ionized gas kinematics, the analysis presented in Kormendy & Ho (2013) for the M-σ relationship omits SMBH mass estimates from gas dynamics except when the mass estimates specifically attempt to incorporate corrections for the high measured dispersions.

It is possible to apply the model presented here to the data omitted in Kormendy & Ho (2013) and reinterpret the M-σ relationship. In Figure 3.8 we reproduce the right side of Figure 12 in Kormendy & Ho (2013) to illustrate the impact of sub-Keplerian accretion flow models on the M-σ relationship. The red, orange, and yellow points represent gas mass estimates assuming the reported measurements, an RIAF-like velocity field, and an ADAF velocity field, respectively. Using the RIAF model, gas dynamics mass estimates could be increased by a factor of two, but this does not dramatically change the slope or scatter of the M-σ relationship, as demonstrated by the orange fit. Using the ADAF

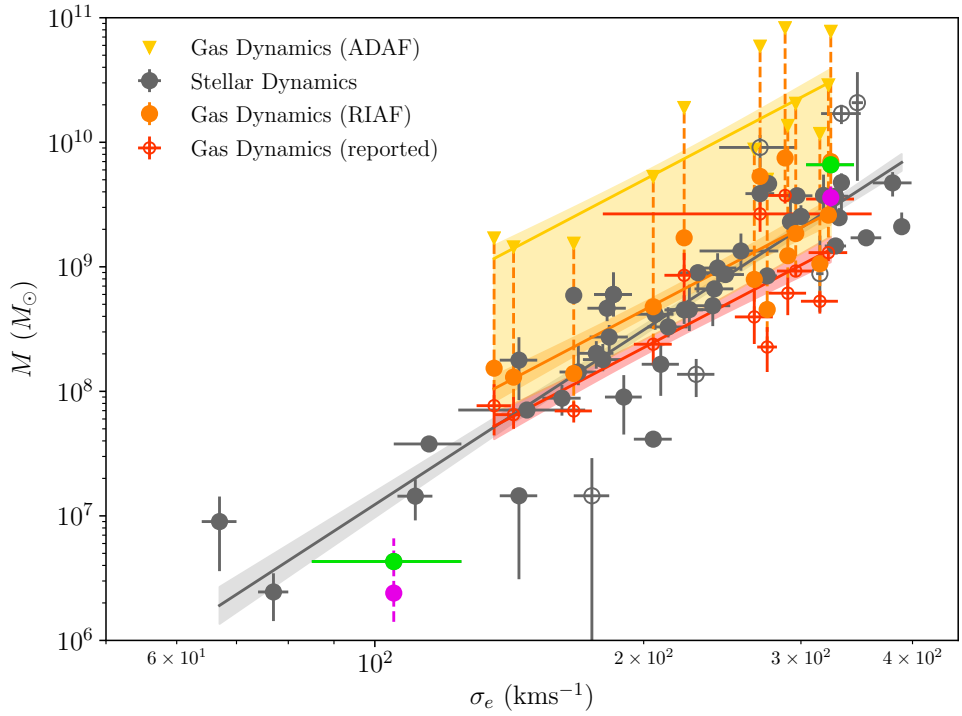

Figure 3.8: M-σ relationship for data collected in Kormendy & Ho (2013). Dark gray points are SMBH mass estimates made using stellar kinematics, and open red points are reported SMBH mass estimates using ionized gas dynamics. Orange points are twice the reported gas dynamics mass estimate, which is possible when assuming the ionized gas follows the slightly sub-Keplerian RIAF model described in this paper. The yellow triangles are 22 times the reported gas dynamics mass estimate, which can arise from assuming the gas is described by the very sub-Keplerian ADAF model from this paper. The gray line is the M-σ fit to the gray points, excluding the open gray points, which are the same as in Kormendy & Ho (2013). The red, orange, and yellow lines are fits to the reported, RIAF, and ADAF gas models, respectively, and the gray, red, and orange shaded regions are the 2 σ confidence regions around each fit. The yellow shaded region spans the breadth of the gas dynamics measurements and represents the worst case scenario for gas dynamics mass estimates. In practice, any change in the mass estimate is likely to be much more modest, and likely lies within the orange band. The green (stellar kinematics) and magenta (gas dynamics) points are the measurements for Sgr A* and M87.

model, the mass estimates would increase by an order of magnitude, and increase the scatter in the relationship in the high dispersion regime, and produce some of the highest estimates for central black hole masses. Such large black hole masses seem unreasonable, so the yellow shaded region should be interpreted as the most pessimistic region for an estimated mass shift. In practice, each object should be individually reanalyzed with this sub-Keplerian model, and any shift in the estimated mass is expected to lie within the orange and red bands. As $M \propto \langle v \rangle^2$, small or moderate changes in the line-of-sight velocity from radial and sub-Keplerian motion can produce significant changes in the estimate of the central mass. For ionized gas-dynamics, the largest systematic when estimating the SMBH mass comes from assumptions about the gas velocity model. Presently, stellar kinematics mass estimates dominate the trend in M-σ, but the advent of high resolution radio interferometry from projects like ALMA should produce many more gas dynamical SMBH mass estimates in the future. Developing gas velocity models that can account for the sub-Keplerian systematic will be important for producing mass estimates consistent with the stellar kinematics estimates.

The gas velocity model presented here makes it possible to simultaneously estimate the mass of the central black hole and characterize the motion of ionized gas in the gravitational influence of the central black hole. This makes it possible to look for trends in gas motion across the mass regime, which may provide insight into why the M-σ relationship saturates at high masses, relative to the M-$L_{\rm bulge}$ relationship.

3.7.3 Applicability to other Gas Dynamics Techniques

Much of the analysis in this work concerns possible systematics when converting ionized gas velocity and dispersion measurements to black hole mass estimates. Many recent studies have made black hole mass estimates using molecular gas velocity measurements using instruments like ALMA to great success (Boizelle et al., 2019). Since ALMA observations are able to measure gas velocities at every resolution element, one can fully map out the velocity structure of circumnuclear molecular gas disks. This is in contrast with the slit spectra method used in ionized gas measurements, where one axis (typically the x-axis) has much lower resolution than the other axis in the image plane, compromising our ability to map the full spatial velocity structure.

In well resolved ALMA systems, the clues that would point towards a more complicated velocity model generally don't exist. These systems generally have very weak to nonexistent AGN activity, their velocity dispersions are typically much lower than in ionized gas systems, and in many cases there exists a clear well-structured gas torus at other observing frequencies. All these various features suggest that the molecular gas disks in these

systems more closely trace the underlying black hole potential without needing significant virial components in their velocity model, and the molecular gas velocities are very well described by thin, Keplerian models.

A common addition to both ionized and molecular gas dynamics velocity models is a tilted or warped gas disk, generally invoked to explain kinematic residuals or "twists" in the innermost regions of the gas disk (Neumayer et al., 2007; Boizelle et al., 2019). These warped disks are typically motivated by an asymmetric or perturbed galactic potential, but efforts to find either the physical source of such asymmetries or quantitatively estimate the amount of warp in the inner disk have not been successful. Since warped disks appear in practice as a change in disk inclination with radius, one could imagine altering the disk thickness with radius to achieve a similar effect.

Megamasing disks around AGN are also famously well described by thin, Keplerian molecular gas disks, but may also contain warped disks (Zhao et al., 2018; Pesce et al., 2020). These warps are similarly motivated by perturbed galactic potentials, but they could also arise from a dynamic, and small, radial velocity component that changes with radius. If the disk was tilted by only a few degrees, with a small but non-negligeble thickness, a small raidal velocity component can produce what looks like a warped masing disk in the image plane, since the addition of radial velocities changes the masing gain path to prefer a different line of sight.

Chapter 4

Conclusions

The publication of the April 2017 observations of M87* mark the start of a new era in AGN research. For the first time, we have made observations of the immediate region of the event horizon, well within the regime necessary to make independent measurements of strong gravity. One of the immediately applicable results from this first set of observations was the measurement of the angular diameter of the black hole shadow to be 42 ± 3 μas. When calibrated against a library of hundreds of GRMHD simulations, this angular diameter corresponds to a mass of 6.5×10^9 $M_\odot$, assuming a distance of 16.8 Mpc to M87 (Event Horizon Telescope Collaboration et al., 2019d,e,f).

The EHT mass estimate of M87* is inconsistent with mass estimates derived from ionized gas dynamics models using thin, Keplerian gas disks. It is possible to resolve the tension between the gas dynamics and the EHT/stellar kinematics mass estimate by introducing additional dynamic freedoms to previously restricted gas dynamics models. The work described in this thesis explores three such freedoms: (1) modifications to the assumed inclination, (2) modifications to the rotational velocity to allow sub-Keplerian motion, and (3) modifications to the vertical disk structure to allow for non-trivial disk thickness. As long as the gas disk is optically thin and inclined with respect to the observer, an increased disk height serves to bias line-of-sight velocities to larger radii, suppressing the effective line-of-sight velocity. This suppression allows for a higher intrinsic disk inclination, and with disk heights of $\approx h = 1/3$ one can just resolve the discrepancy between the EHT and gas dynamics mass estimates without requiring a substantially sub-Keplerian velocity profile. All three dynamic freedoms could be present in M87 to modest degree, and could resolve the tension between the gas dynamics mass estimate and the EHT mass estimate.

Of note, there are no combinations of gas disk inclination and sub-Keplerian factor that,

to within 1σ, align the axis of the ionized gas disk with the axis of the large scale radio jet. Using typical values for the jet and disk inclinations yields a misalignment around 15°, and any non-trivial disk thickness tends to further misalign the large-scale gas disk with the mas jet.

A misalignment between the gas disk and jet could imply some measure of variability due to torques acting between the jet and accretion disk. There already exists some evidence for a semi-periodic oscillation of the jet with an approximate timescale of a decade (Mertens et al., 2016a), and evidence for changes in the jet direction at kpc scales. However, it is not clear at what radii and timescales jet-disk torques should act since they depend strongly on the precise density and fluid profile of the disk. By observing and characterizing the variability in M87's jet, it may be possible to constrain where the torques due to the jet-disk misalignment appear. By using variability measurements of the jet at multiple scales, it will be possible to map the movement of gas from the outer edges of the SMBH sphere of influence all the way to the event horizon.

Beyond the jet and horizon-scale physics, the EHT observations of M87* have already helped resolve a long-standing tension in AGN research. By making an independent mass estimate of the central black hole, we can already make important statements about the structure of ionized gas at radii of 10^4 r_g from the black hole. The angular momentum of this gas must be misaligned with the jet axis, and the EHT mass estimate can support a wide range of possible disk thicknesses, inclinations, and/or sub-Keplerian factors. Such a wide swath of parameter can be pared down by directly comparing our gas dynamics model to either existing or future gas velocity data.

The efforts to model horizon-scale jet variability as described in this paper may produce valuable constraints on the jet-launching structure when compared to the EHT observations. The results of the launch parameter survey in Chapter 2 showed that there are clear structural differences in both the simulated images and light curves between black hole and wind-driven spots. Black-hole driven spots shear faster than wind-driven spots, leading to shorter spot half-lives, multi-modal light curves, and arc-like structures in the simulated images. Black hole driven spots only enhance the light curve for a few days, but wind-driven spots can contribute to the light curve for well over a week. Changing the azimuthal launch position of the spot can increase the maximum intensity to between 2 and 5 times the quiescent intensity. By using a combination of the image morphology, light curve structure, and light curve half-life, it should be possible to distinguish between black hole and wind-driven spots, and shed some light on the structure of the jet-launching region.

GRMHD models have been the focus of the first set of M87* analyses, but model com-

parison frameworks designed for the EHT are now sophisticated and powerful enough to compare fully radiative semi-analytic models directly to the visibility data. The incorporation of time-variable jet models like this one into the model-comparison frameworks will help us to fill in the gaps left un-modeled by GRMHD simulations, and help us understand how giant relativistic jets are formed.

While the horizon-scale light curve for M87* is very uncertain, we should be able to compare it to our models for shearing spots in jets. The time-scale for the slight rise and fall in the M87* light curve (Event Horizon Telescope Collaboration et al., 2019d,f) is similar to that found in some of the shearing spot models, which suggest a model-comparison effort may be able to constrain the space of allowed shearing spot models, and thus the appropriate jet launching mechanism. With multiple observations over the coming years, we will be able to construct a catalogue of horizon-scale light curves which will allow us to check the consistency of variability in M87*.

The focus of much of my research has been to produce simple, extensible models for unsolved problems in AGN astrophysics. M87 is an ideal laboratory to test such models, since its special combination of size and distance mean we can observe nearly every physical scale, from the intra-cluster medium all the way down to the SMBH horizon.

The force-free jet model used as the basis for the velocity and magnetic field in the shearing spot model is already undergoing validation tests in the THEMIS model comparison framework, but the shearing spot model itself will require some optimization to properly utilize high-performance computing. Incorporating more sophisticated jet models like Pu & Takahashi (2020) could also produce different shearing profiles, and it will be important to determine how generic the shearing spot diagnostics are in describing the jet-launching structure.

In the future, it should be straightforward to compare my extended gas dynamics model directly to ionized gas observations of M87, either using the existing measurements from Walsh et al. (2013), or from new observations of the M87 nuclear region. Directly comparing the extended gas dynamics model to real velocity data will be a critical validation test, and open up the possibility of applying the model to other SMBH systems with ionized gas mass estimates.

Achieving precise and accurate black hole mass estimates are critical to understanding the relationship between AGN feedback and galactic evolution. ALMA black hole mass estimates have improved dramatically over earlier ionized gas mass estimates, but well-structured molecular disks appear in only 10% of galaxies. A flexible model for gas dynamics should help to account for some of the systematics present in lower resolution, but much more common, ionized gas mass estimates.

If the EHT images can constrain M87*'s jet to be black-hole driven, driven by a Blandford-Znajek type process, then the jet inclination seen at large scales should be strongly tied to the black hole spin direction. If we apply that to other AGN jet systems, then that means observations of the jet at pc or kpc scales can give us a direct handle on fundamental properties of the black hole at horizon scales. By studying the effects of misalignment between the black hole and accretion disk angular momentum, it may be possible to connect cooling gas from the AGN feedback cycle to the pc scale gas disk that forms the outer edger of the black hole accretion disk, helping to fill in a critical step in our understanding of AGN activity, and the life-cycle of supermassive black holes.

References

Bardeen, J. M., & Petterson, J. A. 1975, ApJ, 195, L65

Barth, A. J., Sarzi, M., Ho, L. C., et al. 2001, in Astronomical Society of the Pacific Conference Series, Vol. 249, The Central Kiloparsec of Starbursts and AGN: The La Palma Connection, ed. J. H. Knapen, J. E. Beckman, I. Shlosman, & T. J. Mahoney, 370

Becklin, E. E., Gatley, I., & Werner, M. W. 1982, ApJ, 258, 135

Beckmann, V., Gehrels, N., Shrader, C. R., & Soldi, S. 2006, ApJ, 638, 642

Bicknell, G. V., & Begelman, M. C. 1996, ApJ, 467, 597

Bird, S., Harris, W. E., Blakeslee, J. P., & Flynn, C. 2010, A&A, 524, A71

Blandford, R. D., & Begelman, M. C. 1999, MNRAS, 303, L1

Blandford, R. D., & Königl, A. 1979, ApJ, 232, 34

Blandford, R. D., & McKee, C. F. 1982, ApJ, 255, 419

Blandford, R. D., & Payne, D. G. 1982, MNRAS, 199, 883

Blandford, R. D., & Znajek, R. L. 1977, MNRAS, 179, 433

Boizelle, B. D., Barth, A. J., Walsh, J. L., et al. 2019, arXiv e-prints, arXiv:1906.06267

Broderick, A., & Blandford, R. 2004, MNRAS, 349, 994

Broderick, A. E., Gold, R., Karami, M., et al. 2020, ApJ, 897, 139

Broderick, A. E., & Loeb, A. 2005, MNRAS, 363, 353

—. 2006a, ApJ, 636, L109

—. 2006b, MNRAS, 367, 905

—. 2009, ApJ, 697, 1164

Broderick, A. E., Narayan, R., Kormendy, J., et al. 2015, ApJ, 805, 179

Bromberg, O., & Levinson, A. 2009, ApJ, 699, 1274

Burkert, A., & Tremaine, S. 2010, ApJ, 720, 516

Cantiello, M., Blakeslee, J. P., Ferrarese, L., et al. 2018, ApJ, 856, 126

Cappellari, M., Neumayer, N., Reunanen, J., et al. 2009, MNRAS, 394, 660

Chan, C.-H., & Krolik, J. H. 2017, ApJ, 843, 58

Davies, R. I., Thomas, J., Genzel, R., et al. 2006, ApJ, 646, 754

Davis, T. A., Bureau, M., Onishi, K., et al. 2017, MNRAS, 468, 4675

de Francesco, G., Capetti, A., & Marconi, A. 2006, A&A, 460, 439

Dexter, J., & Fragile, P. C. 2011, ApJ, 730, 36

Dexter, J., McKinney, J. C., & Agol, E. 2012, MNRAS, 421, 1517

Doeleman, S. S., et al. 2008, Nature, 455, 78

Doeleman, S. S., Fish, V. L., Schenck, D. E., et al. 2012, Science, 338, 355

Eckart, A., Genzel, R., Ott, T., & Schödel, R. 2002, MNRAS, 331, 917

Event Horizon Telescope Collaboration, Akiyama, K., Alberdi, A., et al. 2019a, ApJ, 875, L1

—. 2019b, ApJ, 875, L2

—. 2019c, ApJ, 875, L3

—. 2019d, ApJ, 875, L4

—. 2019e, ApJ, 875, L5

—. 2019f, ApJ, 875, L6

Fabian, A. C. 2012, ARA&A, 50, 455

Ferrarese, L. 2002, ApJ, 578, 90

Ferrarese, L., & Merritt, D. 2000, ApJ, 539, L9

Fragile, P. C., & Anninos, P. 2005, ApJ, 623, 347

Gebhardt, K., Adams, J., Richstone, D., et al. 2011, ApJ, 729, 119

Gebhardt, K., & Richstone, D. O. 2000, in Bulletin of the American Astronomical Society, Vol. 32, American Astronomical Society Meeting Abstracts #196, 700

Gebhardt, K., Bender, R., Bower, G., et al. 2000, ApJ, 539, L13

Genzel, R., Eisenhauer, F., & Gillessen, S. 2010, Reviews of Modern Physics, 82, 3121

Ghez, A., Morris, M., Lu, J., et al. 2009, in Astronomy, Vol. 2010, astro2010: The Astronomy and Astrophysics Decadal Survey

Gillessen, S., Eisenhauer, F., Fritz, T. K., et al. 2009a, ApJ, 707, L114

Gillessen, S., Eisenhauer, F., Trippe, S., et al. 2009b, ApJ, 692, 1075

Giroletti, M., Hada, K., Giovannini, G., et al. 2012, A&A, 538, L10

Gold, R., Broderick, A. E., Younsi, Z., et al. 2020, ApJ, 897, 148

Hada, K., Doi, A., Kino, M., et al. 2011, Nature, 477, 185

Hada, K., Kino, M., Doi, A., et al. 2016, ApJ, 817, 131

Harris, G. L. H., & Harris, W. E. 2011, MNRAS, 410, 2347

Hawley, J. F., & Krolik, J. H. 2006, ApJ, 641, 103

Imanishi, M., Nakanishi, K., & Izumi, T. 2018, ApJ, 856, 143

Irons, W. T., Lacy, J. H., & Richter, M. J. 2012, ApJ, 755, 90

Jeter, B., Broderick, A. E., & McNamara, B. R. 2019, ApJ, 882, 82

Jones, T. W., & Odell, S. L. 1977, ApJ, 214, 522

Junor, W., Biretta, J. A., & Livio, M. 1999, Nature, 401, 891

Kormendy, J., & Bender, R. 2011, Nature, 469, 377

Kormendy, J., & Ho, L. C. 2013, ARA&A, 51, 511

Kormendy, J., & Richstone, D. 1995, ARA&A, 33, 581

Lacy, J. H., Baas, F., Townes, C. H., & Geballe, T. R. 1979, ApJ, 227, L17

Lacy, J. H., Townes, C. H., Geballe, T. R., & Hollenbach, D. J. 1980, ApJ, 241, 132

Ly, C., Walker, R. C., & Junor, W. 2007, ApJ, 660, 200

Lynden-Bell, D. 1969, Nature, 223, 690

Macchetto, F., Marconi, A., Axon, D. J., et al. 1997, ApJ, 489, 579

Marconi, A., & Hunt, L. K. 2003, ApJ, 589, L21

Mazzucchelli, C., Bañados, E., Venemans, B. P., et al. 2017, ApJ, 849, 91

McKinney, J. C. 2006, MNRAS, 368, 1561

McKinney, J. C., Tchekhovskoy, A., & Blandford, R. D. 2012, MNRAS, 423, 3083

McNamara, B. R., & Nulsen, P. E. J. 2012, New Journal of Physics, 14, 055023

Mertens, F., Lobanov, A. P., Walker, R. C., & Hardee, P. E. 2016a, A&A, 595, A54

—. 2016b, A&A, 595, A54

Meyer, E. T., Sparks, W. B., Biretta, J. A., et al. 2013, ApJ, 774, L21

Montero-Castaño, M., Herrnstein, R. M., & Ho, P. T. P. 2009, ApJ, 695, 1477

Mościbrodzka, M., Falcke, H., & Shiokawa, H. 2016, A&A, 586, A38

Narayan, R., Mahadevan, R., & Quataert, E. 1998, in Theory of Black Hole Accretion Disks, ed. M. A. Abramowicz, G. Björnsson, & J. E. Pringle, 148–182

Narayan, R., & Yi, I. 1994, ApJ, 428, L13

—. 1995, ApJ, 444, 231

Natarajan, P., & Armitage, P. J. 1999, MNRAS, 309, 961

Natarajan, P., & Pringle, J. E. 1998, ApJ, 506, L97

Neumayer, N., Cappellari, M., Reunanen, J., et al. 2007, ApJ, 671, 1329

Padmanabhan, T. 2000, Theoretical Astrophysics - Volume 1, Astrophysical Processes, 622, doi:10.2277/0521562406

Park, M.-G., & Ostriker, J. P. 1999, ApJ, 527, 247

Pastorini, G., Marconi, A., Capetti, A., et al. 2007, A&A, 469, 405

Pesce, D. W., Braatz, J. A., Reid, M. J., et al. 2020, ApJ, 890, 118

Peterson, B. M., & Bentz, M. C. 2011, Black-hole masses from reverberation mapping, ed. M. Livio & A. M. Koekemoer, 100–111

Petrosian, V., & McTiernan, J. M. 1983, Phys. of Fluids, 26, 3023

Press, W. H., Teukolsky, S. A., Vetterling, W. T., & Flannery, B. P. 2007, Numerical Recipes 3rd Edition: The Art of Scientific Computing, 3rd edn. (New York, NY, USA: Cambridge University Press)

Prieto, M. A., Fernández-Ontiveros, J. A., Markoff, S., Espada, D., & González-Martín, O. 2016, MNRAS, 457, 3801

Pu, H.-Y., & Takahashi, M. 2020, ApJ, 892, 37

Quataert, E., & Narayan, R. 1999, ApJ, 516, 399

Schödel, R., Ott, T., Genzel, R., et al. 2002, Nature, 419, 694

Schwarzschild, K. 1916, Sitzungsberichte der Königlich Preußischen Akademie der Wissenschaften (Berlin, 189

Seyfert, C. K. 1943, ApJ, 97, 28

Shakura, N. I., & Sunyaev, R. A. 1973, A&A, 24, 337

Shen, Y. 2013, Bulletin of the Astronomical Society of India, 41, 61

Sparks, W. B., Biretta, J. A., & Macchetto, F. 1996, ApJ, 473, 254

Stawarz, Ł., Aharonian, F., Kataoka, J., et al. 2006, MNRAS, 370, 981

Tan, J. C., Beuther, H., Walter, F., & Blackman, E. G. 2008, ApJ, 689, 775

Tchekhovskoy, A., McKinney, J. C., & Narayan, R. 2008, MNRAS, 388, 551

Verdoes Kleijn, G. A., van der Marel, R. P., de Zeeuw, P. T., Noel-Storr, J., & Baum, S. A. 2002, AJ, 124, 2524

Walker, R. C., Hardee, P. E., Davies, F., et al. 2016, Galaxies, 4, 46

Walsh, J. L., Barth, A. J., Ho, L. C., & Sarzi, M. 2013, ApJ, 770, 86

Walsh, J. L., Barth, A. J., & Sarzi, M. 2010, ApJ, 721, 762

Walsh, J. L., van den Bosch, R. C. E., Barth, A. J., & Sarzi, M. 2012, ApJ, 753, 79

Young, A. J., Wilson, A. S., & Mundell, C. G. 2002, ApJ, 579, 560

Yuan, F., Quataert, E., & Narayan, R. 2003, ApJ, 598, 301

Zhao, W., Braatz, J. A., Condon, J. J., et al. 2018, ApJ, 854, 124

Zhu, L., Long, R. J., Mao, S., et al. 2014, ApJ, 792, 59